AGU PUBLICATIONS

JGR

Journal of Geophysical Research: Space Physics

RESEARCH ARTICLE

10.1002/2014JA019876

Key Points:
- ULF indices contain nonsinusoidal periodic signals in universal time
- ULF indices are not the strongest correlator with radiation belt electron fluxes
- ULF indices were integrated into a mathematical system science of magnetosphere

Correspondence to:
J. E. Borovsky,
jborovsky@spacescience.org

Citation:
Borovsky, J. E., and M. H. Denton (2014), Exploring the cross correlations and autocorrelations of the ULF indices and incorporating the ULF indices into the systems science of the solar wind-driven magnetosphere, *J. Geophys. Res. Space Physics*, *119*, 4307–4334, doi:10.1002/2014JA019876.

Received 10 FEB 2014
Accepted 7 MAY 2014
Accepted article online 12 MAY 2014
Published online 2 JUN 2014

Exploring the cross correlations and autocorrelations of the ULF indices and incorporating the ULF indices into the systems science of the solar wind-driven magnetosphere

Joseph E. Borovsky[1,2,3] and Michael H. Denton[2,3]

[1]Atmospheric, Oceanic, and Space Sciences Department, University of Michigan, Ann Arbor, Michigan, USA, [2]Center for Space Plasma Physics, Space Science Institute, Boulder, Colorado, USA, [3]Department of Physics, Lancaster University, Lancaster, Lancashire, UK

Abstract The ULF magnetospheric indices S_{gr}, S_{geo}, T_{gr}, and T_{geo} are examined and correlated with solar wind variables, geomagnetic indices, and the multispacecraft-averaged relativistic-electron flux F in the magnetosphere. The ULF indices are detrended by subtracting off sine waves with 24 h periods to form S_{grd}, S_{geod}, T_{grd}, and T_{geod}. The detrending improves correlations. Autocorrelation-function analysis indicates that there are still strong 24 h period nonsinusoidal signals in the indices which should be removed in future. Indications are that the ground-based indices S_{grd} and T_{grd} are more predictable than the geosynchronous indices S_{geod} and T_{geod}. In the analysis, a difference index $\Delta S_{mag} \approx S_{grd} - 0.693\ S_{geod}$ is derived: the time integral of ΔS_{mag} has the highest ULF index correlation with the relativistic-electron flux F. In systems-science fashion, canonical correlation analysis (CCA) is used to correlate the relativistic-electron flux simultaneously with the time integrals of (a) the solar wind velocity, (b) the solar wind number density, (c) the level of geomagnetic activity, (d) the ULF indices, and (e) the type of solar wind plasma (coronal hole versus streamer belt): The time integrals of the solar wind density and the type of plasma have the highest correlations with F. To create a solar wind-Earth system of variables, the two indices S_{grd} and S_{geod} are combined with seven geomagnetic indices; from this, CCA produces a canonical Earth variable that is matched with a canonical solar wind variable. Very high correlations ($r_{corr} = 0.926$) between the two canonical variables are obtained.

1. Introduction

The ULF indices S_{gr}, S_{geo}, T_{gr}, and T_{geo} are 1 h resolution measurements of the amplitude of magnetic field fluctuations in the 2–8 min timescale as determined by ground magnetometers in the dawn-dayside sectors (S_{gr} and T_{gr}) and as determined by spacecraft in geosynchronous orbit (S_{geo} and T_{geo}).

From a systems science point of view, long-term parameters (indices) that describe the state of the magnetospheric system are valuable. Systems science of the magnetosphere has largely relied on the use of geomagnetic indices to describe the reaction of the magnetosphere to the solar wind [cf. *Vassiliadis*, 2006; *Valdivia et al.*, 2013]; these various geomagnetic indices are indicators of the intensity of latitude currents (*AE*, *AL*, *AU*, polar cap index (PCI)), the strength of magnetospheric convection (*Kp*, midnight boundary index (MBI)), and plasma pressure in the inner magnetosphere (*Dst*, *Dst**). Recently, the ULF indices have been proposed as such systems-science parameters [*Romanova et al.*, 2007; *Kozyreva et al.*, 2007; *Romanova and Pilipenko*, 2009; *Singh et al.*, 2013].

The ULF index is also relevant to the evolution of the outer electron radiation belt [*Kozyreva et al.*, 2007; *Romanova et al.*, 2007; *Romanova and Pilipenko*, 2009], since there is a well-known statistical connection between the amplitudes of ULF waves and the energization and radial diffusion of relativistic electrons in the magnetosphere [*Rostoker et al.*, 1998; *Mathie and Mann*, 2000; *Friedel et al.*, 2002; *Nakamura et al.*, 2002; *Elkington et al.*, 2003; *Degeling et al.*, 2011].

In this report we will explore the ULF index and incorporate it into a composite Earth variable composed of multiple geomagnetic indices plus the ground-based and geosynchronous ULF indices. Detrended ULF indices S_{grd}, S_{geod}, T_{grd}, and T_{geod} will be produced by subtracting off universal time sine wave functions. Correlations between the ULF indices and the solar wind will be explored, correlations between the ULF indices and solar wind driver functions for the magnetosphere will be examined, correlations between the

ULF indices and other geomagnetic indices will be investigated, and correlations between the ULF indices and relativistic-electron fluxes will be explored. To examine the driving of the ULF indices by the solar wind and to investigate the connections of the ULF indices to other geomagnetic indices, the mathematical technique of canonical correlation analysis (CCA) will be utilized. CCA is useful for exploring global correlation patterns in multivariable data sets such as the combined solar wind, geomagnetic index, ULF index, and radiation belt data set. One pattern repeatedly found involves differences between the ground-based ULF index and the geosynchronous ULF index. This will lead to the definition and analysis of a differential ULF index $\Delta S_{mag} \equiv S_{grd} - 0.693 S_{geod}$. The ULF indices will be integrated into the data set of geomagnetic indices to form an Earth data set, and the global correlations between the Earth data set and the solar wind data set will be explored with CCA. CCA will generate a single time series Earth variable $E_{(1)}$ and CCA will generate a solar wind driver function $S_{(1)}$ for that Earth variable. For times when the ULF indices are not available, formulas for generating proxies to the ULF indices will be developed.

This paper is organized as follows. In section 2, the ULF data sets are described and the sine wave detrending of the ULF indices is performed. Section 3 describes cross correlations of the ULF indices with the solar wind, with solar wind driver functions, and with geomagnetic indices. Section 4 analyzes autocorrelation functions of the ULF indices and compares them with autocorrelation functions of the solar wind and geomagnetic indices. Section 5 uses canonical correlation analysis to investigate the connections of the ULF indices to the solar wind, to geomagnetic indices, and to the relativistic-electron flux in the magnetosphere. In section 6, the ULF indices are combined with the geomagnetic indices to form an Earth data set and canonical correlation analysis is used to connect that Earth data set to the solar wind data set. The findings of this study are summarized in section 7. Section 8 contains a discussion of some of the properties of the ULF indices and of future work including future improvements to the ULF indices. In Appendix A, proxy formulas for the ULF indices are given.

2. The ULF Wave Indices

The ULF indices S_{gr}, S_{geo}, T_{gr}, and T_{geo} are measurements of the spectral power of magnetic field fluctuations within the magnetosphere in the 2–7 mHz (143–500 s) frequency band. The S index refers to “signal” power and the T index refers to “total” power: The S index is created from the T index by subtracting off a noise floor in a Fourier transform [cf. *Kozyreva et al.*, 2007].

The ground ULF indices S_{gr} and T_{gr} are created from measurements from ground-based magnetometers in the 5–15 LT sector (dawnside and dayside) and in the 60°–70° region of magnetic latitude in the Northern Hemisphere. The geosynchronous ULF indices S_{geo} and T_{geo} are created from magnetic field measurements on board the GOES spacecraft [*Singer et al.*, 1996] in geosynchronous orbit (6.6 R_E) in the equatorial magnetosphere.

Two additional ULF indices in the solar wind will be utilized in the present study: T_{imf} and T_{den}. T_{imf} is the spectral power of magnetic field fluctuations (in the spacecraft frame) in the 2–7 mHz frequency range constructed from magnetic field measurements in the solar wind upstream of the Earth. T_{den} is a measure of solar wind number-density fluctuations (in the spacecraft frame) in a broader frequency range constructed from density measurements in the solar wind upstream of the Earth.

All six ULF indices S_{gr}, S_{geo}, T_{gr}, T_{geo}, T_{imf}, and T_{den} are available at 1 h time resolution in the years 1991–2004 at http://virbo.org/Augsburg/ULF [cf. *Kozyreva et al.*, 2007; *Romanova et al.*, 2007].

In the present study, the magnetospheric ULF indices S_{gr}, S_{geo}, T_{gr}, and T_{geo} are each detrended by subtracting a sine wave in universal time UT from each index. The sine waves were determined by regression fitting the entire 1991–2004 databases of S_{gr}(UT), S_{geo}(UT), T_{gr}(UT), and T_{geo}(UT) values. Those detrended indices S_{grd} and S_{geod} are given by

$$S_{grd} = S_{gr} - 1.065 - 0.07957 \sin(2\pi[\mathrm{UT} + 16.784]/24) \quad (1a)$$

$$S_{geod} = S_{geo} + 0.1415 + 0.07563 \sin(2\pi[\mathrm{UT} + 5.676]/24) \quad (1b)$$

and the detrended indices T_{grd} and T_{geod} are given by

$$T_{grd} = T_{gr} - 0.87889 - 0.08391 \sin(2\pi[\mathrm{UT} + 16.097]/24) \quad (2a)$$

$$T_{geod} = T_{geo} + 0.3732 - 0.07292 \sin(2\pi[\mathrm{UT} + 6.072]/24) \quad (2b)$$

where the universal time UT is given in hours and where the sine functions operate on radians. (Further UT trends in the indices are discussed in section 8.2.)

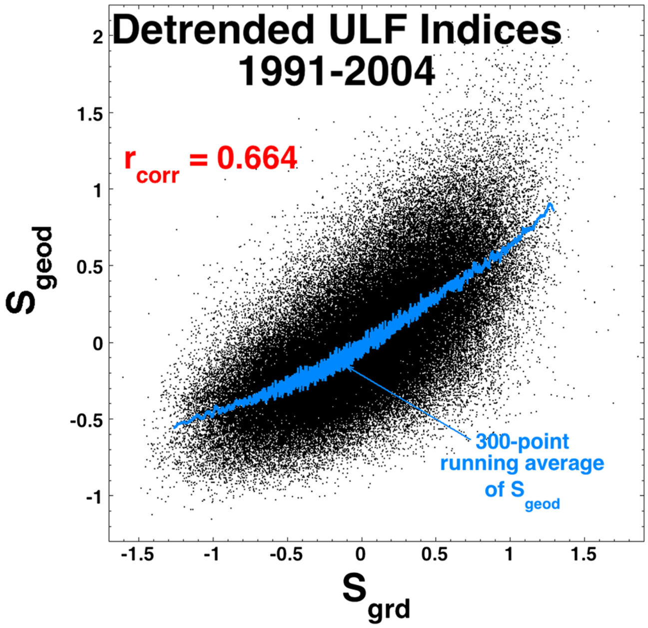

Figure 1. Hourly averaged values of the detrended geosynchronous ULF index S_{geod} are plotted as a function of the hourly averaged values of the detrended ground-based index S_{grd}.

In Figure 1, 122,736 hourly values of the detrended index S_{geod} are plotted in black as a function of S_{grd}. A 300-point running average of S_{geod} is plotted in blue. The running average highlights the trend underlying the black points. The blue curve is fairly straight, indicating an approximately linear relationship between S_{geod} and S_{grd} under the noise. As indicated on the figure, the Pearson linear correlation coefficient [*Bevington and Robinson*, 1992, equation (11.17)] between S_{geod} and S_{grd} is $r_{corr} = 0.664$. This means that $r_{corr}^2 = 44\%$ of the variance of S_{geod} can be described by the variance of S_{grd}, or conversely that 44% of the variance of S_{grd} can be described by the variance of S_{geod}. Note that the linear correlation coefficient between the nondetrended indices S_{gr} and S_{geo} is $r_{corr} = 0.639$, which have only 41% of the variance in common.

A plot of T_{geod} versus T_{grd} looks very similar to the plot of Figure 1, with a linear correlation coefficient of $r_{corr} = 0.640$. For the nondetrended values, the correlation between T_{geo} and T_{gr} is $r_{corr} = 0.618$. Note that the correlation between T_{grd} and S_{grd} is $r_{corr} = 0.986$ and the correlation between T_{geod} and S_{geod} is $r_{corr} = 0.985$.

3. Cross Correlations With the ULF Indices

In this section, linear correlations between the four detrended ULF indices S_{grd}, S_{geod}, T_{grd}, and T_{geod} and solar wind and geomagnetic variables are examined.

3.1. Correlations With the Solar Wind

In Table 1, the Pearson linear correlation coefficients r_{corr} are collected between various solar wind quantities and (a) the detrended ground ULF index S_{grd}, (b) the detrended geosynchronous ULF index S_{geod}, (c) the detrended ground ULF index T_{grd}, (d) the detrended geosynchronous ULF index T_{geod}, and (e) the difference ULF index $\Delta S_{mag} = S_{grd} - 0.693 S_{geod}$. For the majority of the solar wind quantities, the correlations are calculated using the OMNI2 [*King and Papitashvili*, 2005] hourly averaged solar wind values for the years 1991–2004; for the O^{7+} to O^{6+} and the C^{6+} to C^{5+} charge-state density ratios of the solar wind plasma, hourly averaged values from the ACE Solar Wind Ion Composition Spectrometer (SWICS) instrument [*Gloeckler et al.*, 1998] in the years 1998–2004 are used. In Table 1, the values of the ULF indices are evaluated at the same hour as the solar wind parameters. The notation $<X>_3$ means a 3 h average of the quantity X using the hour of the ULF indices and the two prior hours. In general, for magnetic field orientation quantities, correlations are much higher if a 3 h average is used [cf. *Borovsky*, 2013a].

In the first and third columns of Table 1, it is seen that the ground-based ULF indices S_{grd} and T_{grd} are relatively strongly correlated with the solar wind speed v_{sw}, the proton temperature T_p, the ram pressure $n v_{sw}^2$, and with the clock angle function $<\sin^2(\theta_{clock}/2)>_3$ and they are relatively strongly anticorrelated with $<B_z>_3$. The correlations of the ULF indices with v_{sw} and B_z have been reported before [*Romanova et al.*, 2007; *Kozyreva et al.*, 2007] and the correlation between ULF activity and v_{sw} is well known [e.g., *Singer et al.*, 1977; *Mathie and Mann*, 2001; *Pahud et al.*, 2009]. Since v_{sw} and T_p are strongly correlated in the solar wind ($r_{corr} = 0.63$), it is likely that the correlation of the ULF index with T_p is a proxy for correlation with v_{sw} (i.e., it is likely that T_p and the ULF indices are not causally related to each other). In Table 1, S_{grd} and T_{grd} are modestly correlated with $<\delta B_{vec}>_3$ and $<T_{imf}>_3$, where $<\delta B_{vec}>_3$ is the amplitude of the fluctuation of the magnetic

Table 1. Collected Pearson Linear Correlation Coefficients Between Five ULF Indices and Various Solar Wind Parameters[a]

	S_{grd}	S_{geod}	T_{grd}	T_{geod}	ΔS_{mag}
n	−0.019	+0.211	−0.018	+0.205	−0.186
v_{sw}	+0.527	+0.444	+0.540	+0.437	+0.359
$\log(nv^2)$	+0.331	+0.531	+0.340	+0.518	+0.034
T_p	+0.366	+0.357	+0.368	+0.349	+0.212
α/p	−0.103	+0.138	+0.109	+0.139	+0.033
B_{mag}	+0.295	+0.478	+0.295	+0.470	+0.022
B_x	−0.033	−0.026	−0.033	−0.025	−0.023
B_y	−0.034	+0.005	−0.040	−0.002	−0.050
$<B_z>_3$	−0.427	−0.320	−0.393	−0.301	−0.320
$<\sin^2(\theta_{clock}/2)>_3$	+0.471	+0.310	+0.434	+0.292	+0.387
$<\theta_{Bn}>_3$	−0.039	+0.095	+0.028	+0.090	+0.024
θ_{tilt}	−0.034	+0.005	−0.040	−0.002	−0.050
M_A	−0.089	−0.076	−0.083	−0.077	−0.056
v_A	+0.222	+0.222	+0.222	+0.222	+0.122
$\log(S_p)$	+0.325	+0.184	+0.326	+0.181	+0.288
$\log(C^{6+}/C^{5+})$	−0.253	−0.208	−0.262	−0.206	−0.175
$\log(O^{7+}/O^{6+})$	−0.228	−0.108	−0.230	−0.108	−0.220
$F_{10.7}$	−0.002	+0.090	+0.007	+0.109	−0.075
$<\delta B_{vec}>_3$	+0.395	+0.532	+0.395	+0.521	+0.116
$<\delta B_{vec}/B>_3$	+0.237	+0.219	+0.236	+0.211	+0.147
$<T_{imf}>_3$	+0.338	+0.385	+0.342	+0.383	+0.150
$<T_{den}>_3$	+0.114	+0.346	+0.115	+0.339	+0.115

[a]Here $\Delta S_{mag} \equiv S_{grd} - 0.693 S_{geod}$. Note that S_p is the proton-specific entropy of the solar wind $T_p/n^{2/3}$.

field vector of the solar wind. Owing to the intercorrelations of the solar wind variables, correlation with $<\delta B_{vec}>_3$ (and with $<T_{imf}>_3$) could be a proxy for correlation with v_{sw}, B_{mag}, and/or nv_{sw}^2 [cf. *Borovsky and Funsten*, 2003].

The values in the second and fourth columns of Table 1 show that the geosynchronous ULF indices S_{geod} and T_{geod} are relatively strongly correlated with v_{sw}, T_p, $\log(nv^2)$, and B_{mag} and they are modestly anticorrelated with $<B_z>_3$. S_{geod} and T_{geod} are also strongly correlated with $<\delta B_{vec}>_3$ and modestly correlated with $<T_{imf}>_3$ and $<T_{den}>_3$.

Comparing the values in the S_{grd} and T_{grd} columns with the values in the S_{geod} and T_{geod} columns of Table 1, it is seen that geosynchronous ULF amplitudes S_{geod} and T_{geod} are more strongly correlated with n, $\log(nv^2)$, B_{mag}, $<\delta B_{vec}>_3$, and $<T_{den}>_3$ than are the ground-based ULF amplitudes S_{grd} and T_{grd}. Conversely, the ground-based amplitudes S_{grd} and T_{grd} are more strongly correlated with v_{sw}, $<B_z>_3$, and $<\sin^2(\theta_{clock}/2)>_3$ than are the geosynchronous amplitudes S_{geod} and T_{geod}.

Note in Table 1 that the correlations for S_{grd} and S_{geod} are in general larger than the correlations for T_{grd} and T_{geod}. This indicates that the signal ULF indices S_{grd} and S_{geod} are more accurate (and perhaps more fundamental) than the total ULF indices T_{grd} and T_{geod}.

In the final column of Table 1 are the correlation coefficients r_{corr} for the difference $\Delta S_{mag} = S_{grd} - 0.693 S_{geod}$. The strengths of the correlations with ΔS_{mag} are weaker than the strengths for S_{grd} or S_{geod}. The strongest correlations for ΔS_{mag} are for $<\sin^2(\theta_{clock}/2)>_3$ and for v_{sw}.

3.2. Correlations With Solar Wind Driver Functions

In Table 2, the Pearson linear correlation coefficients r_{corr} between the ULF indices S_{grd}, S_{geod}, T_{grd}, T_{geod}, and $\Delta S_{mag} = S_{grd} - 0.693 S_{geod}$ and seven solar wind driver functions in the literature are collected. The first three driver functions are based on the solar wind electric field, the fourth and fifth driver functions are derivations of the dayside reconnection rate, and the last two driver functions are reconnection drivers with viscous drivers added. More or less, the correlation coefficients increase going down the table. The first row (with the poorest correlation coefficients) is for $-v_{sw}B_z$ [*Rostoker et al.*, 1972] (with B_z in GSM coordinates), the second row is for $v_{sw}B_s$ [*Holzer and Slavin*, 1982] (where $B_s = -B_z$ for $B_z < 0$ and $B_s = 0$ for $B_z \geq 0$, again in GSM), and the third row is the Newell function $v_{sw}^{4/3} B_\perp^{2/3} \sin^{8/3}(\theta_{clock}/2)$ [*Newell et al.*, 2007] where $B_\perp = (B_y^2 + B_z^2)^{1/2}$. In the

Table 2. Collected Pearson Linear Correlation Coefficients Between Five ULF Indices and Seven Different Solar Wind Driver Functions for the Magnetosphere[a]

		S_{grd1}	S_{geod1}	T_{grd1}	T_{geod1}	ΔS_{mag1}
1	$-v_{sw}B_z$	0.375	0.285	0.344	0.267	0.278
2	$v_{sw}B_z$	0.451	0.451	0.430	0.432	0.254
3	Newell	0.569	0.542	0.545	0.521	0.341
4	R_{quick}	0.582	0.588	0.561	0.568	0.321
5	R_2	0.588	0.596	0.567	0.576	0.322
6	$\mathcal{G};+\mathcal{B}$	0.684	0.682	0.670	0.660	0.384
7	$NL(\mathcal{G}+\mathcal{B})$	0.710	0.691	0.696	0.670	0.411

[a]The ULF indices are lagged by 1 h from the time of the solar wind.

fourth row, R_{quick} is the simplified "quick" derivation of the reconnection control function $R_{\text{quick}} = n^{1/2}v_{sw}^2 \sin^2(\theta_{\text{clock}}/2)\, M_A^{-1.35}\, [1 + 680M_A^{-3.30}]^{-1/4}$ [*Borovsky and Birn*, 2014] (where M_A is the Alfven Mach number of the upstream solar wind flow) and in the fifth row, R_2 is the full derivation of the reconnection control function [*Borovsky*, 2013b]. In the last two rows of Table 2, G stands for the reconnection-coupled MHD generator, which mathematically accounts for polar cap potential saturation in the coupling between the solar wind and the magnetosphere, and B is a viscous interaction driver function based on Bohm diffusion [*Borovsky*, 2013a]. The *NL* in the last row indicates that the driver function is nonlinear, having been parameterized to account for the nonlinear mathematical relationship between the strength of magnetospheric convection and the strength of solar wind driving.

In all cases in Table 2, there is a 1 h lag between the evaluation of the solar wind driver function with measured solar wind parameters and the values of the ULF indices (with the ULF indices evaluated the hour after the solar wind). This is noted in the column labels by the subscript 1. This 1 h lag is demonstrated in Figure 2 where the correlation coefficients r_{corr} between the ULF indices S_{grd} and S_{geod} and the seven driver functions are plotted three times: once for 0 h time lag (green), once for 1 h time lag (red), and once for 2 h time lag (blue). For all seven drivers and for both ULF indices, the 1 h lag produces greater correlations than the 0 h or 2 h lags. Plots for T_{grd} and T_{geod} look almost identical to the S_{grd} and S_{geod} plots of Figure 2. This 1 h time lag is interpreted as the reaction time of the ULF indices to the solar wind. Most geomagnetic indices also respond to the solar wind with about a 1 h time lag [cf. *McPherron et al.*, 1986; *Borovsky*, 2008].

In the first four columns of Table 2 and in Figure 2, there is a wide range of correlation coefficients r_{corr} between the solar wind driver functions and the ULF indices S_{grd}, S_{geod}, T_{grd}, and T_{geod}. This wide range is also true when the driver functions are compared with geomagnetic indices [cf. *Borovsky*, 2013a]. The most

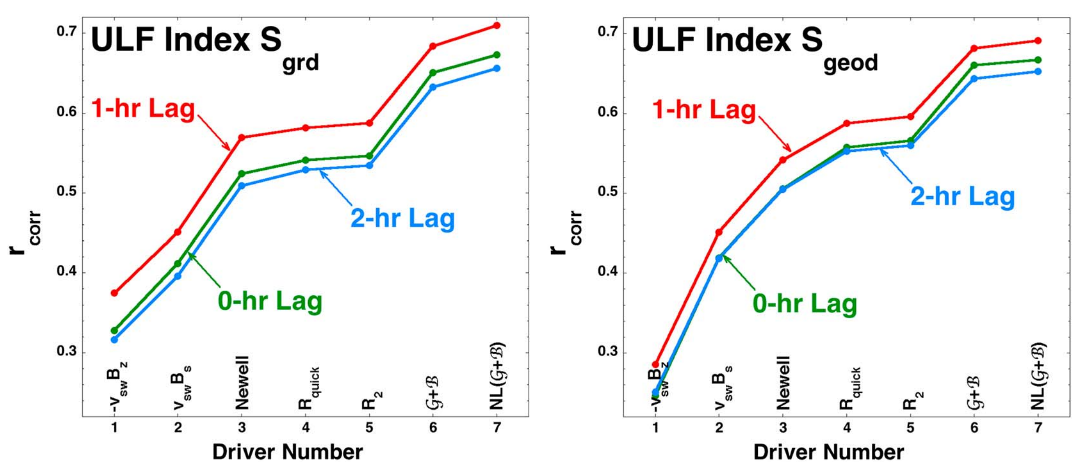

Figure 2. The Pearson linear correlation coefficients of (left) S_{grd} and (right) S_{geod} are plotted for seven different solar wind driver functions. The green curves are for no time lag between the ULF indices and the driver functions, the red curves are for the ULF indices lagged 1 h behind the driver functions, and the blue curves are for the ULF indices lagged 2 h behind the driver functions.

Table 3. Collected Pearson Linear Correlation Coefficients Between Five ULF Indices and Eight Geomagnetic Indices and the Relativistic Electron Flux *F*

	S_{grd}	S_{geod}	T_{grd}	T_{geod}	ΔS_{mag}
Kp	0.736	0.759	0.724	0.739	0.389
−MBI	0.729	0.732	0.711	0.714	0.401
−*Dst*	0.490	0.482	0.482	0.472	0.276
−*Dst**	0.553	0.611	0.550	0.598	0.265
AE	0.710	0.652	0.685	0.630	0.438
−*AL*	0.683	0.606	0.659	0.583	0.439
AU	0.605	0.602	0.585	0.583	0.338
PCI	0.626	0.584	0.603	0.565	0.378
F	0.061	−0.143	0.061	−0.152	0.191

commonly used driver functions $-v_{sw}B_z$ and $v_{sw}B_s$ produce poor correlations. The amount of variance in the ULF indices that can be described by the driver function is $r_{corr}{}^2$: For the $-v_{sw}B_z$ driver, the $r_{corr}{}^2$ values for S_{grd}, S_{geod}, T_{grd}, and T_{geod} are range from 0.071 to 0.118: This is only 7.1% to 11.8% of the variance of ULF indices that can be accounted for by the driver function $-v_{sw}B_z$. In contrast, for the $NL(\mathcal{G}+\mathcal{B})$ driver function the $r_{corr}{}^2$ values with S_{grd}, S_{geod}, T_{grd}, and T_{geod} are from 0.670 to 0.710: This is 44.9% and 50.4% of the variance of the ULF indices that can be accounted for by the driver function $NL(\mathcal{G}+\mathcal{B})$. The relatively high correlations between the superior driver functions and the ULF indices imply that there is a relationship between the reconnection driving of the magnetosphere and the amplitudes of ULF waves measured at geosynchronous orbit and on the ground.

Again in Table 2, the correlation coefficients of S_{grd} and S_{geod} are larger than the correlation coefficients of T_{grd} and T_{geod}. This again implies that the signal indices S_{grd} and S_{geod} are more accurate (and perhaps more fundamental) than are the total indices T_{grd} and T_{geod}.

The final column of Table 2 contains the correlation coefficients r_{corr} between the difference $\Delta S_{mag1} = S_{grd1} - 0.693 S_{geod1}$ and the solar wind driver functions. The correlations with ΔS_{mag1} are weaker than the correlations for S_{grd1} and for S_{geod1}.

3.3. Correlations With Geomagnetic Indices

In Table 3, the Pearson linear correlation coefficients r_{corr} between the ULF indices S_{grd}, S_{geod}, T_{grd}, T_{geod}, and $\Delta S_{mag} = S_{grd} - 0.693 S_{geod}$ and eight geomagnetic indices are collected. In Table 3, there is no time lag between the value of the geomagnetic index and the value of the ULF index. Zero time lag produces the best correlations between the ULF indices and *AE*, PCI, *AL*, *AU*, and *Kp*. A 1 h time lag between MBI and the ULF indices produces the best correlations, with MBI measured the hour following the ULF indices. A 1 h time lag between *Dst** and the ULF indices produces the best correlations, with *Dst** measured the hour following the ULF indices. And a 2 h time lag between *Dst* and the ULF indices produces the best correlations, with *Dst* measured 2 h following the ULF indices. Longer time lags for *Dst* are typical as *Dst* has a slow response to solar wind driving [cf. *Smith et al.*, 1999].

The correlation coefficients between S_{grd}, S_{geod}, T_{grd}, and T_{geod} and the geomagnetic indices in the first four columns of Table 3 are fairly strong. The coefficients are particularly strong for the two geomagnetic indices *Kp* and MBI, in the range 0.711–0.759. *Kp* and MBI are both measures of the depth of penetration of the electron plasma sheet into the dipolar regions of the magnetosphere on the nightside [*Gussenhoven et al.*, 1983; *Thomsen*, 2004], which are measures of the strength of plasma convection in the magnetosphere. Note that the correlation coefficient between the ground-based ULF index S_{grd} and the geosynchronous orbit ULF index S_{geod} is $r_{corr} = 0.664$ (cf. Figure 1); hence, these two ULF indices are each correlated to *Kp* more strongly than they are correlated to each other. Likewise for T_{grd} and T_{geod}, they are each correlated to *Kp* more strongly than they are correlated to each other.

In Table 3, the correlation coefficients of S_{grd}, S_{geod}, T_{grd}, and T_{geod} with the set of indices *AE*, *AL*, *AU*, and PCI are also fairly strong, in the range 0.583–0.710, with *AU* being the poorest. These four indices are measures of the strengths of high-latitude currents (with *AE* algebraically defined as $AE = AU - AL$).

The correlation of S_{grd}, S_{geod}, T_{grd}, and T_{geod} with Dst* is also fairly strong in Table 3. Dst* is a measure of the plasma diamagnetism in the inner magnetosphere [*Dessler and Parker*, 1959], produced by ions with orbits trapped in the dipolar magnetosphere [*Sckopke*, 1966] and by plasma flowing past the dipole from the nightside to the dayside [*Liemohn et al.*, 2001]. Note in Table 3 that the correlations of the ULF indices with the pressure-corrected index Dst* are significantly higher than with the uncorrected Dst index. Here the formula $Dst^* = Dst - 20.7P_{\rm ram} + 27.7$ [*Borovsky and Denton*, 2010a] is used to produce Dst* from Dst, where the solar wind ram pressure $P_{\rm ram} = m_p n v_{sw}{}^2$ is in units of nPa.

In Table 3, the magnitudes of the correlation coefficients of S_{grd} and S_{geod} are larger than those of T_{grd} and T_{geod}. This again implies that the signal indices S_{grd} and S_{geod} are more accurate (and perhaps more fundamental) than are the total indices T_{grd} and T_{geod}.

In the final column of Table 3, the correlation coefficients between $\Delta S_{mag} = S_{grd} - 0.693S_{geod}$ and the geomagnetic indices are about half of the values of the correlation coefficients between S_{grd} and S_{geod} and the geomagnetic indices.

In the bottom row of Table 3, the correlation coefficients between ULF indices and the multispacecraft-averaged logarithm of the 1.1–1.5 MeV electron flux F at geosynchronous orbit are displayed. The fluxes were measured by the Synchronous Orbit Particle Analyzer [*Belian*, 1999] in circular geosynchronous orbits at the geographic equator. For each year of data, the 1.1–1.5 MeV flux measurements on each of seven spacecraft in operation were normalized so that all spacecraft had the same yearly averaged logarithm of the flux in the dawn sector. Half-hour running averages of the measurements on each satellite were used to construct a multispacecraft logarithmic average (sum of log fluxes divided by number satellites) of all the available fluxes at any time. The multispacecraft-averaged flux F was cleaned by removing times of known solar-energetic-particle events. This multispacecraft-averaged flux has been used in prior studies of the radiation belt dynamics [cf. *Borovsky and Denton*, 2009a, 2010a; *Denton et al.*, 2010]. In the bottom row of Table 3, the correlation coefficients between the ULF indices S_{grd}, S_{geod}, T_{grd}, T_{geod}, and ΔS_{mag} and the relativistic-electron flux F are quite low. In section 5.3, it will be seen that the correlations between F and time integrals of the ULF indices can be quite high, especially for the time integral of the difference $\Delta S_{mag} = S_{grd} - 0.693S_{geod}$.

4. Autocorrelation Functions of the ULF Indices

In this section, temporal autocorrelation functions of the ULF indices are examined and compared with autocorrelation functions of various solar wind and geomagnetic quantities.

In Figure 3 (top), autocorrelation functions of S_{grd} (blue) and S_{geod} (red) are plotted. The autocorrelation function is a measure of persistence in the time series. The autocorrelation function $A(\tau_{\rm shift})$ of a variable $X(t)$ is

$$A(\tau_{\rm shift}) = \int X(t)X(t-\tau_{\rm shift})\mathrm{d}t / \int X(t)X(t)\mathrm{d}t \quad (3)$$

where $\tau_{\rm shift}$ is a time shift in the data set. For $\tau_{\rm shift} = 0$, the autocorrelation function is unity. Note the local peaks in the autocorrelation functions at multiples of 24 h, particularly for S_{grd}. These peaks indicate the presence in the time series of a signal with a 24 h period. Note in Figure 3 that sinusoidal signals with 24 h periods were already subtracted off S_{gr} and S_{geo} to make S_{grd} and S_{geod} (cf. expressions (1a), (1b), (2a), and (2b)). The remaining signals with 24 h periodicity are not sinusoidal. Undoubtedly, fitting those 24 h signals and subtracting them out of S_{grd} and S_{geod} would produce ground-based and geosynchronous ULF indices with less noise and higher correlations with solar wind parameters and with other geomagnetic indices. Those improved ULF indices will also better correlate with the relativistic-electron flux in the magnetosphere. Figure 3 shows peaks at 27 days: There is a well-known periodicity in the solar wind and in geomagnetic activity at the solar rotation period of 27 days [cf. *Borovsky*, 2013a, Figure 13].

The rate of falloff of the autocorrelation function from unity is known as the autocorrelation time. To get the autocorrelation times, here the 1/e method will be used, denoting the time shift $\tau_{\rm shift}$ where the autocorrelation function crosses $1/e = 0.368$ as the autocorrelation time. Fitting S_{grd} and S_{geod} curves to eliminate their first peaks at 24 h and taking the 1/e crossing time of the fitted curves, the autocorrelation time for S_{grd} is 11 h and the autocorrelation time for S_{geod} is 14 h.

Also plotted in green in Figure 3 (top) is the autocorrelation function of the difference $\Delta S_{mag} = S_{grd} - 0.693S_{geod}$, which is $S_{grd}{}^* - 0.569S_{geod}{}^*$ where the asterisks denote a variable that has been

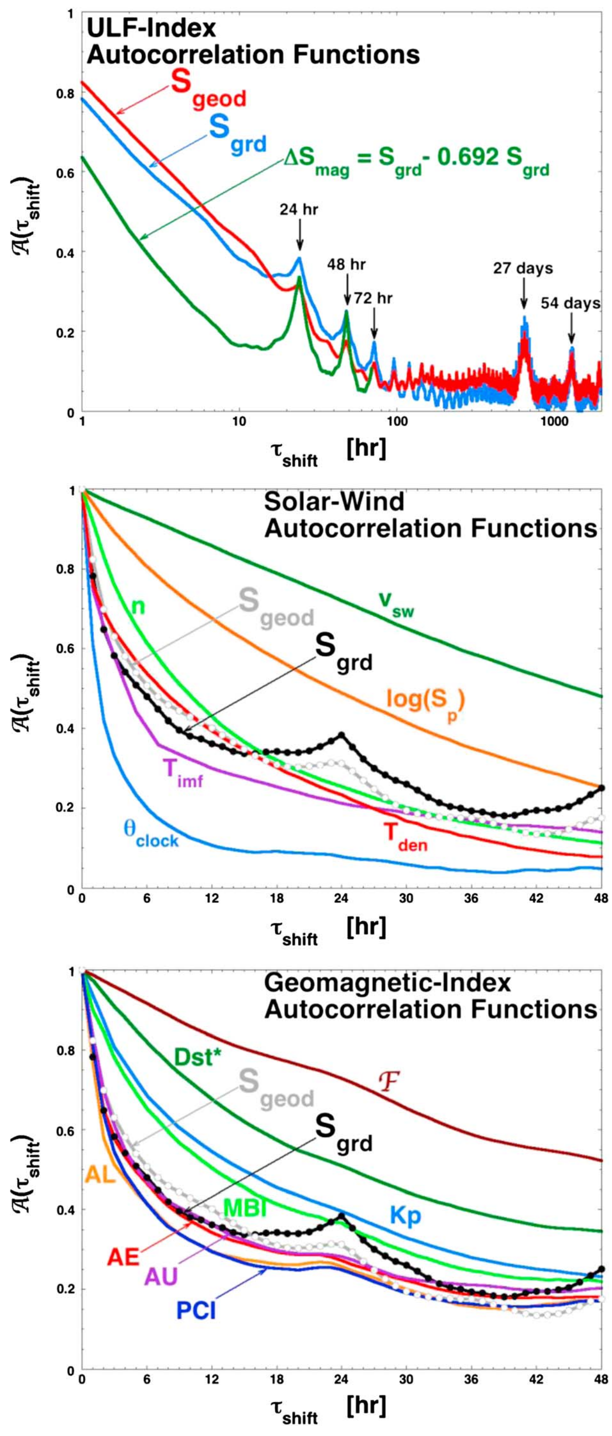

Figure 3. Temporal autocorrelation functions are plotted (top) for the ULF indices S_{grd}, S_{geod}, and ΔS_{mag}, (middle) for various solar wind variables, and (bottom) for geomagnetic indices and the geosynchronous relativistic-electron flux in the bottom panel. In Figure 3 (middle and bottom), the autocorrelation functions of S_{grd} and S_{geod} are replotted in black and gray.

standardized (dimensionless and normalized), which will be defined in section 5. As will be seen in section 5.3, this difference produces the largest correlation with the relativistic-electron flux F at geosynchronous orbit. Note that the 24 h periodic signal dominates the autocorrelation function of ΔS_{mag}. The autocorrelation time (1/e method) of $\Delta S_{mag} = S_{grd} - 0.693 S_{geod}$ is 3 h, which here is a measure of the width of the 24 h peaks.

In Figure 3 (middle), the autocorrelation functions of S_{grd} (black) and S_{geod} (gray) are compared with the autocorrelation functions of various solar wind parameters. The solar wind velocity v_{sw} (green) and the logarithm of the proton-specific entropy S_p (orange) have longer persistence times relative to S_{grd} and S_{geod}, and the interplanetary magnetic field (IMF) clock angle θ_{clock} (blue) has a shorter persistence time. The autocorrelation functions of the solar wind number density n and the solar wind ULF indices T_{den} and T_{imf} have similar behavior to the autocorrelation functions of S_{grd} and S_{geod}. Note, of course, the absence of a 24 h peak in the solar wind quantities.

In Figure 3 (bottom), the autocorrelation functions of S_{grd} (black) and S_{geod} (gray) are compared with the autocorrelation functions of geomagnetic indices and the multispacecraft relativistic-electron flux F. Four curves have persistence times longer than those of S_{grd} and S_{geod}: the relativistic-electron flux F (74 h), Dst* (40 h), Kp (26 h), and MBI (23 h). The geomagnetic indices AL and PCI have autocorrelation times shorter than those of S_{grd} and S_{geod}, both being about 8 h. The autocorrelation functions of AE and AU have behaviors quite similar to the autocorrelation function of S_{grd}, except for the recurring 24 h signal in S_{grd}.

In Figure 4, strong 24 h period signals in S_{grd} and S_{geod} will be removed from the autocorrelation functions to examine the autocorrelation function of the ULF indices without the periodic signals. Since the autocorrelation function $A(\tau_{\text{shift}})$ and the power spectral density are Fourier transform pairs [e.g., *Tennekes and Lumley*, 1972, equation (6.4.20)], eliminating a 24 h periodic signal in the autocorrelation function is equivalent to viewing an autocorrelation function where Fourier filtering of the time series has been performed. In Figure 4 (top), the autocorrelation function of S_{grd} is plotted in green. At integer multiples of 24 h,

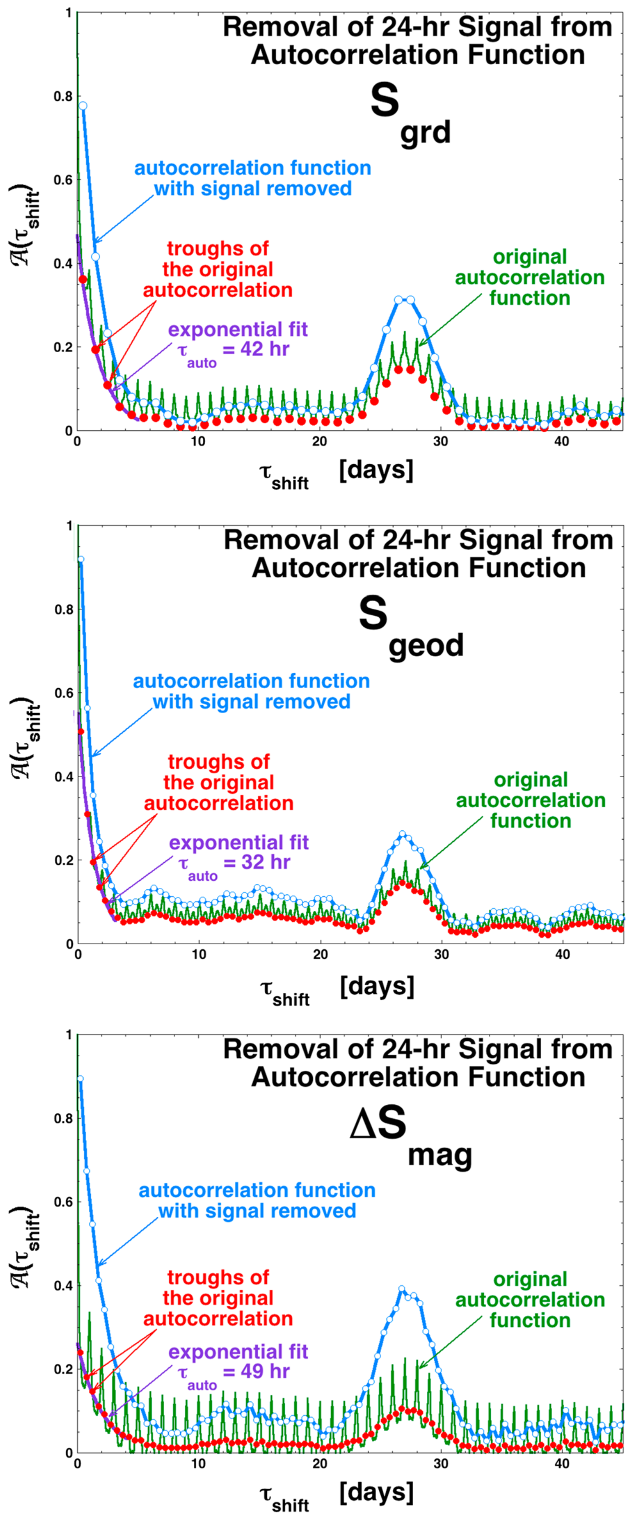

Figure 4. The removal of 24 h period and 12 h period signals from the autocorrelation functions of (top) S_{grd}, (middle) S_{geod}, and (bottom) ΔS_{mag} is shown.

there are peaks in the autocorrelation function with flat trough regions between the peaks. The half-day values of the autocorrelation function are plotted as the red points in Figure 4 (top). These red points indicate the temporal behavior of the autocorrelation function in the absence of the 24 h periodic signal. However, the red-point autocorrelation function is not normalized so that its value is unity at $\tau_{shift} = 0$. To obtain the normalization, the red points are fit with an exponential function over the first few days of τ_{shift}. That exponential fit to the red points is plotted in Figure 4 (top) as the purple curve, which has the functional form 0.466 exp($-0.578\tau_{shift}$). At $\tau_{shift} = 0$, the value of this function is 0.466. Dividing the red-point autocorrelation function by 0.466 yields the normalized autocorrelation function with the 24 h signal removed; this cleaned autocorrelation function is plotted in blue in Figure 4 (top). The cleaned autocorrelation function of S_{grd} has an autocorrelation time of 42 h.

In Figure 4 (middle), the process is repeated for the autocorrelation function of S_{geod}. Looking at the original autocorrelation function plotted in green in the figure, it can be noted that instead of wide flat troughs between the 24 h peaks there are subpeaks. These subpeaks represent the presence of a 12 h period signal in the S_{geod} time series. To avoid these subpeaks, instead of taking the troughs to be located at the half days, the troughs are taken to be located at the quarter days. The quarter-day points of the autocorrelation function are plotted in red in Figure 4 (middle). These red points are fit within exponential function over the first few days of τ_{shift} and that fit is plotted in purple in Figure 4 (middle): Its functional form is 0.551 exp ($-0.751\tau_{shift}$). Dividing the red-point autocorrelation function by 0.551, the normalized cleaned autocorrelation function of S_{geod} is plotted in blue in Figure 4 (middle). This cleaned autocorrelation function has an autocorrelation time of 32 h.

The process is repeated again for the difference ULF index $\Delta S_{mag} = S_{grd} - 0.693 S_{geod}$ in Figure 4 (bottom). Again, the quarter-day values of the autocorrelation function are used for the troughs since the difference index ΔS_{mag} involves S_{geod} which has the secondary peaks. Fitting the red-point autocorrelation with an

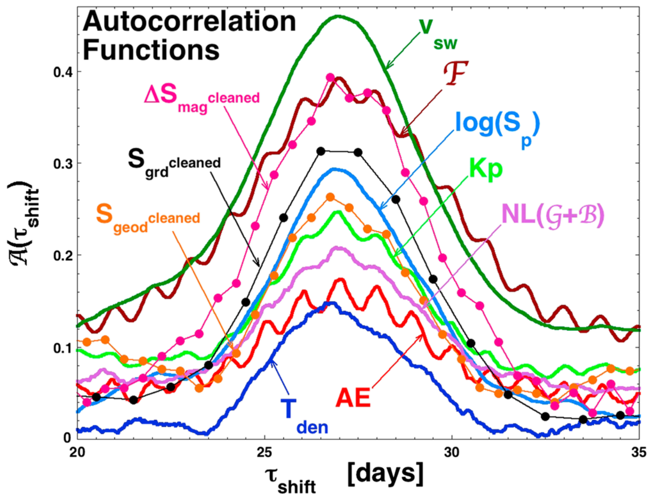

Figure 5. The 27 day local maximum in the autocorrelation functions of various quantities is examined.

exponential function over the first few days of τ_{shift} (plotted in purple) yields the functional form 0.268 exp ($-0.494\tau_{shift}$). Dividing the red-point autocorrelation by 0.268 results in the normalized cleaned autocorrelation function of ΔS_{mag} that is plotted in blue in Figure 4 (bottom). The autocorrelation time of the cleaned autocorrelation function of ΔS_{mag} is 49 h. In all three cases (S_{grd}, S_{geod}, and ΔS_{mag}), the autocorrelation times of the cleaned functions are substantially longer than the autocorrelation times of the original functions, which were 11 h for S_{grd}, 14 h for S_{geod}, and 3 h for ΔS_{mag}: The autocorrelation times of the original functions are strongly affected by the autocorrelation time of the 24 h and 12 h periodic signals in the time series. Note in Figure 4 that the 27 day peaks of the cleaned autocorrelation functions (blue curves) are all substantially larger than the 27 day peaks of the original autocorrelation functions (green curves).

In Figure 5 the cleaned autocorrelation functions of S_{grd} (black with points), S_{geod} (orange with points), and ΔS_{mag} (pink with points) are compared with some of the other autocorrelation functions around the 27 day peak. Note in Figure 5 that all Earth-based measurements show a 1 day periodicity in their autocorrelation functions and that solar wind measurements do not. Note the very large amplitude of the 27 day recurrence peak in the relativistic-electron flux F (brown). A similar large amplitude is seen in the solar wind velocity v_{sw} (green) and nearly as large in the logarithm of the proton-specific entropy log(S_p) (blue). Note that the magnitude of the 27 day peak in the cleaned autocorrelation function of ΔS_{mag} is quite large, about the same as the peak in the autocorrelation function of F and similar to the peaks for log(S_p) and v_{sw}.

5. Investigating the ULF Indices With Canonical Correlation Analysis

Recently canonical correlation analysis has been used to statistically explore solar wind/magnetosphere coupling (J. E. Borovsky, Canonical correlation analysis of the combined solar-wind and geomagnetic-index data sets, submitted to *Journal of Geophysical Research*, 2013c; The coupling strength of solar-wind/magnetosphere interaction through the solar cycle examined with an accurate driver function: No dependence on the phase of the solar cycle, submitted to *Journal of Geophysical Research*, 2013d). In this section, canonical correlation analysis will be utilized to compare various data sets to gain insights into the properties of the ULF indices and their connections to solar wind variables, geomagnetic indices, and the relativistic-electron flux in the magnetosphere.

Canonical correlation analysis (CCA) mathematically finds patterns of correlation between two multivariate data sets [cf. *Muller*, 1982; *Johnson and Wichern*, 2007; *Gatignon*, 2010; *Nimon et al.*, 2010]. When applied to Data Set 1 and Data Set 2, CCA creates a new set of variables $A_{(1)}$, $A_{(2)}$, $A_{(3)}$, … that are linear combinations of the original variables from Data Set 1 and CCA creates a new set of variables $B_{(1)}$, $B_{(2)}$, $B_{(3)}$, … that are linear combinations of the original variables from Data Set 2. The pair $A_{(1)}$ and $B_{(1)}$ are the "first canonical variables" of the combined data set and the correlation coefficient $r_{(1)}$ between them is the "first canonical correlation" between the two data sets. Likewise the pair $A_{(2)}$ and $B_{(2)}$ are the second canonical variables and the correlation between them $r_{(2)}$ is the second canonical correlation. Variables $A_{(2)}$ and $B_{(2)}$ are completely uncorrelated with variables $A_{(1)}$ and $B_{(1)}$; hence, the $A_{(2)} \leftrightarrow B_{(2)}$ correlation in the combined data set is completely unrelated to the $A_{(1)} \leftrightarrow B_{(1)}$ correlation.

All variables going into the CCA processes must be standardized so that each is given the same weighting. The standardization of the variables is performed by subtracting off the mean value of the variable and

Table 4. Formulas Used to Obtain the Hourly Averaged Dimensionless Normalized Variables From the Hourly Averaged Variables in the Years 1991–2004[a]

Variable	Units	Formula
S_{grd}	nT	$S_{grd}* = 2.114 S_{grd} - 0.00740$
S_{geod}	nT	$S_{geod}* = 2.573 S_{geod} + 0.0614$
T_{grd}	nT	$T_{grd}* = 2.11 T_{grd} - 0.00717$
T_{geod}	nT	$T_{geod}* = 2.44 T_{geod} + 0.00566$
AE	nT	$\log(AE)* = 0.996 \log(AE) - 4.91$
AU	nT	$AU* = 0.0136 AU - 1.146$
AL	nT	$AL* = 0.00637 AL + 0.872$
PCI		$\text{PCI}* = 0.961\text{PCI} - 1.071$
Kp	none	$Kp* = 0.723 Kp - 1.618$
MBI	deg	$\text{MBI}* = 0.5685\text{MBI} + 35.77$
$Dst*$	nT	$Dst** = 0.0388 Dst* + 0.676$
v_{sw}	km/s	$v_{sw}* = 0.00984 v_{sw} - 4.368$
n	cm^{-3}	$\log(n)* = 1.496 \log(n) - 2.523$
nv_{sw}^2	cm^{-3} k/s	$\log(nv_{sw}^2)* = 1.756 \log(nv_{sw}^2) - 24.278$
B_{mag}	nT	$B_{mag}* = 0.3134 B_{mag} - 2.057$
B_z	nT	$B_z* = 0.2968 B_z + 0.0464$
$<\sin^2(\theta_{clock}/2)>_3$	none	$<\sin^2(\theta_{clock}/2)>_3* = 3.949<\sin^2(\theta_{clock}/2)>_3 - 2.044$
$<\theta_{Bn}>_3$	deg	$<\theta_{Bn}>_3* = 0.05717<\theta_{Bn}>_3 - 3.022$
S_p	eV cm^{-2}	$S_p* = 0.2360 S_p - 0.9412$
M_A	none	$\log(M_A)* = 2.351 \log(M_A) - 4.805$
$F_{10.7}$	SFU	$\log(F_{10.7})* = 2.704 \log(F_{10.7}) - 12.91$
θ_{clock}	deg	$\theta_{clock}* = 0.02294\theta_{clock} - 2.119$
T_{imf}		$T_{imf}* = 2.751 T_{imf} + 1.017$
T_{den}		$T_{den}* = 3.117 T_{den} + 2.274$

[a]The variables marked by an asterisk have zero mean value and a standard deviation of unity.

dividing by the standard deviation of the variable. This also makes the variable dimensionless. For example, for use in CCA, the solar wind number density n will be transformed to $n* = (n - \langle n\rangle)/\sigma(n)$ where $\langle n\rangle$ is the mean value of n and $\sigma(n)$ is the standard deviation of n. If the natural (base-e) logarithm of n is used, then log (n) will be normalized into $\log(n)* = [\log(n) - \langle\log(n)\rangle]/\sigma(\log(n))$. For the variables used in the present study, the formulas used to generate the normalized variables are collected in Table 4. The asterisk after each variable indicates that that variable is standardized to have zero mean and a standard deviation of unity. When the input variables are all dimensionless and normalized with zero mean and with standard deviations of unity, then all of the canonical variables $A_{(k)}$ and $B_{(k)}$ will also be dimensionless and with zero mean and standard deviations of unity.

With canonical correlation analysis, the number of simultaneous input variables is not limited, so the choice of input variables can be quite complicated. Like simpler statistical methods, what you can interpret depends on the input variables that you use and different sets of input variables yield different results and can be used to study different problems. CCA tends to perform better with input variables that are Gaussian distributed [*Hair et al.*, 2010]. For positive-definite variables that have very skew distributions (such as n or AE), using the logarithm of the variable generally produces higher correlation coefficients in the CCA process. Typically, the variable is tried with and without the logarithm and the form that produces the higher correlation is chosen.

5.1. The ULF Indices and the Solar Wind

In this section, a ULF data set composed of the two variables S_{grd1} and S_{geod1} is compared with a solar wind data set composed of the three variables v_{sw}, $\log(n)$, and $<\sin^2(\theta_{clock}/2)>_3$. The ULF data set is composed of

Table 5. CCA Coefficients (Weights) for a Three-Variable Solar Wind Data Set Matched to a Two-Variable ULF Index Data Set[a]

	Solar Wind Input Variables			ULF Indices		
	$v_{sw}*$	$\log(n)*$	$<\sin^2(\theta_{clock}/2)>_3*$	$S_{grd1}*$	$S_{geod1}*$	Canonical Correlation Coefficient r
First	+1.57	+0.89	+0.91	+1.00	+0.78	0.742
Second	−0.24	−0.87	+0.36	+1.00	−1.05	0.327

[a]The first row is for the first canonical correlation and the second row is for the second canonical correlation.

Table 6. Corresponding to the CCA Case in Table 5, the Correlation Coefficients (Loadings) Between the Individual Solar Wind and ULF Index Input Variables and the Canonical Variables

	Correlation With $S_{(1)}$	Correlation With $U_{(1)}$	Correlation With $S_{(2)}$	Correlation With $U_{(2)}$
v_{sw}	68.4%		25.9%	
log(n)	4.3%		−87.5%	
$<\sin^2(\theta_{clock}/2)>_3$	56.2%		42.4%	
S_{grd1}		93.1%		36.5%
S_{geod1}		88.4%		−47.6%

one ground-based index (S_{grd}) and one geosynchronous index (S_{geod}). The solar wind input parameters explored here are chosen based on prior studies that showed that the amplitudes of fluctuations in the magnetosphere are related to the solar wind velocity [*Singer et al.*, 1977; *Mathie and Mann*, 2001; *Romanova et al.*, 2007; *Kozyreva et al.*, 2007] and to the solar wind density [*Menk et al.*, 2003; *Takahashi and Ukhorskiy*, 2008; *Viall et al.*, 2009], with the clock angle function $\sin(\theta_{clock}/2)$ included as a possible mediator of the coupling. The CCA results appear in Tables 5 and 6: Table 5 contains the coefficients (weights) of the canonical variables and Table 6 contains the correlation coefficients (loadings) r_{corr} between the individual variables and the canonical variables. The two new ULF index canonical variables $U_{(1)}$ and $U_{(2)}$ are a sum of the two ULF indices $U_{(1)} = S_{grd1}^* + 0.78S_{geod1}^*$ and a difference of the two ULF indices $U_{(2)} = S_{grd1}^* - 1.05S_{geod1}^*$. The sum $U_{(1)}$ is described by the new solar wind canonical variable $S_{(1)} = 1.57v_{sw}^* + 0.89\log(n)^* + 0.91 <\sin^2(\theta_{clock}/2)>_3^*$ with a canonical correlation coefficient of 0.742 (Table 5, last column). As can be seen in the first column of Table 6, the correlation of v_{sw} with $S_{(1)}$ is 68.4%, the correlation of log(n) with $S_{(1)}$ is 4.3%, and the correlation of $<\sin^2(\theta_{clock}/2)>_3$ with $S_{(1)}$ is 56.2%. There is almost no correlation between $S_{(1)}$ and log(n). $S_{(1)}$ is dominated by v_{sw} and $\sin^2(\theta_{clock}/2)$; hence, the ULF variable $U_{(1)}$ is dominantly driven by v_{sw} and $\sin^2(\theta_{clock}/2)$. The difference $U_{(2)}$ is described by (cf. Table 5) $S_{(2)} = -0.24v_{sw}^* - 0.87\log(n)^* + 0.36 <\sin^2(\theta_{clock}/2)>_3^*$ with a canonical correlation coefficient of 0.327 (Table 5, last column). The data set utilized is composed of $N = 64{,}910$ hourly averages; correlation at the 95% confidence level occurs for a correlation coefficient with a magnitude larger than $2/N^{1/2} = 0.0078$ [*Beyer*, 1966; *Bendat and Piersol*, 1971], so a correlation of 0.327 is a definite correlation. Note, however, with a coefficient of 0.327, this is not a strong correlation. The third column of Table 6 shows that the correlation of the individual variables with $S_{(2)}$ is dominated by an anticorrelation (−85.7%) with log(n). Hence, the ULF difference variable $U_{(2)}$ is driven by an anticorrelation with log(n) of the solar wind.

The first canonical ULF variable $U_{(1)}$ resulting from the CCA process is $U_{(1)} = S_{grd1}^* + 0.78S_{geod1}^*$. Note that the coefficient 1.0 of S_{grd1}^* is larger in magnitude than the coefficient 0.78 of S_{geod1}^*. The CCA process finds the combination of S_{grd1}^* and S_{geod1}^* that has the maximum correlation with the solar wind data set. This combination emphasizes S_{grd1}^* over S_{geod1}^*. The interpretation of this emphasis is that there is more predictability of S_{grd} from the solar wind than there is for S_{geod}. If a solar wind data set with many more solar wind input variables is used in the CCA process, the resulting combination $U_{(1)}$ still relies more heavily on S_{grd1}^* than on S_{geod1}^*.

If the CCA process is repeated using the total ULF wave power indices T_{grd1} and T_{geod1} instead of S_{grd1} and S_{geod1}, very similar results are obtained.

5.2. The ULF Indices and Geomagnetic Indices

In Table 7, the coefficients (weights) are displayed for a CCA comparing the ULF index data set composed of S_{grd} and S_{geod} with a geomagnetic index data set composed of log(AE), Kp, and MBI. For the ULF index data

Table 7. CCA Coefficients (Weights) Collected for a Three-Variable Geomagnetic Index Data Set Matched to a Two-Variable ULF Index Data Set[a]

	Geomagnetic Indices			ULF Indices		
	log(AE)*	Kp*	MBI*	S_{grd}*	S_{geod}*	Canonical Correlation Coefficient r
First	+0.60	+0.75	+0.35	+1.00	+0.74	0.844
Second	+1.47	−0.86	−0.60	+1.00	−1.07	0.252

[a]The first row is for the first canonical correlation and the second row is for the second canonical correlation.

Table 8. Corresponding to the CCA Case of Table 7, the Correlation Coefficients (Loadings) Between the Individual Geomagnetic Index and ULF Index Input Variables and the Canonical Variables

	Correlation With $G_{(1)}$	Correlation With $U_{(1)}$	Correlation With $G_{(2)}$	Correlation With $U_{(2)}$
log(*AE*)	92.1%		38.8%	
Kp	94.7%		−24.4%	
MBI	91.1%		−13.6%	
S_{grd}		93.6%		35.2%
S_{geod}		87.8%		−47.9%

set, one ground-based index (S_{grd}) and one geosynchronous index (S_{geod}) are chosen, and for the geomagnetic index data set, a mix of high-latitude (log(*AE*)) and convective (*Kp* and MBI) indices is chosen. In Table 8, the correlation coefficients (loadings) between the individual variables and the resulting canonical variables are collected. As was the case of section 5.1 and Table 5, the two new canonical ULF variables $U_{(1)}$ and $U_{(2)}$ are a sum and a difference: The coefficients of the variables $U_{(1)} = S_{grd}^* + 0.74 S_{geod}^*$ and $U_{(2)} = S_{grd}^* - 1.07 S_{geod}^*$ are very similar to the coefficients in Table 5 for the connection of the ULF indices to the solar wind data set. The two corresponding canonical geomagnetic variables $G_{(1)}$ and $G_{(2)}$ are a sum of the three geomagnetic indices $G_{(1)} = 0.60\ \log(AE)^* + 0.75\ Kp^* + 0.35\ \mathrm{MBI}^*$ and a difference $G_{(2)} = 1.47\ \log(AE)^* - 0.86\ Kp^* - 0.60\ \mathrm{MBI}^*$. The first canonical correlation between $U_{(1)}$ and $G_{(1)}$ is 0.844 and the second canonical correlation between $U_{(2)}$ and $G_{(2)}$ is 0.252 with definite correlation at the level $2/(69410)^{1/2} = 0.0078$. Examining the first column of Table 8, it is seen that the individual geomagnetic indices log(*AE*), *Kp*, and MBI all correlate highly with $G_{(1)}$, with the strongest correlation being with *Kp*. In the difference variable $G_{(2)}$, the geomagnetic index with a positive coefficient is a "high-latitude" index log(*AE*) measuring the strength of high-latitude currents and the two geomagnetic indices with negative coefficients are "convective" indices *Kp* and MBI measuring the strength of plasma convection in the magnetosphere [*Gussenhoven et al.*, 1983; *Thomsen*, 2004]. As can be seen by examining the third column in Table 8, log(*AE*) is positively correlated with $G_{(2)}$ and *Kp* and MBI are negatively correlated with $G_{(2)}$. In prior CCA that compared the geomagnetic-index data set to the solar wind data set (J. E. Borovsky, submitted manuscript, 2013c), splitting of the set of geomagnetic indices between high-latitude versus convective indices has also been seen. In the top line (first canonical correlation) of Table 7, the sum $S_{grd}^* + 0.74 S_{geod}^*$ is described by a sum of convective plus high-latitude indices since the coefficients of log(*AE*), *Kp*, and MBI are all positive. In the second line of Table 7 (second canonical correlation), the difference $S_{grd}^* - 1.07 S_{geod}^*$ is described by the strength of the high-latitude indices minus the strength of the convective indices; hence, the difference is statistically larger at times when the high-latitude indices are strong relative to the convective indices.

As was the case for the correlation of the ULF indices with the solar wind in section 5.1 and Table 5, $U_{(1)} = S_{grd}^* + 0.74 S_{geod}^*$ has a larger coefficient for S_{grd}^* than it does for S_{geod}^*. CCA finds the maximum correlation between the ULF indices and geomagnetic indices; the interpretation of the larger coefficient for S_{grd}^* is that there is more predictability of S_{grd} from geomagnetic indices than there is for S_{geod}.

5.3. Relativistic-Electron Flux and Integrals of the ULF Indices

The relativistic-electron population of the outer electron radiation belt is dynamic, with rapid losses [*Freeman*, 1964; *Nagai*, 1988; *Onsager et al.*, 2002] and rapid recoveries [*Borovsky and Denton*, 2009a] and with slow losses [*Meredith et al.*, 2006; *Borovsky and Denton*, 2009b] and slow heating phases [*Nagai*, 1988; *Baker et al.*, 1990; *Borovsky et al.*, 1998]. Using correlation analysis, the time derivatives (temporal changes) of the radiation belt flux will be examined (Tables 9 and 10) and then the flux values themselves will be examined (Figures 6 and 7). The analysis of the changes in the flux will provide insight into the direct analysis of the flux.

The shorter-term versus longer-term behavior of the temporal changes of the relativistic-electron flux is investigated in Tables 9 and 10. In Table 9, the coefficients (weights) of the CCA highest-correlation vector $V_{(1)}$ are displayed and in Table 10 the correlation coefficients (loadings) r_{corr} (in percent) between the CCA highest-correlation vector $V_{(1)}$ and the variables that constitute $V_{(1)}$. In the various rows of Tables 9 and 10, the temporal change in the relativistic-electron flux *F* is compared with (a) the ULF indices S_{grd} and S_{geod}, (b) the solar wind quantities v_{sw}, n, $\log(S_p)$, and $\sin^2(\theta_{clock})$, and (c) the geomagnetic indices log(*AE*) and *Kp*. The

Table 9. Canonical Correlation Analysis Is Used to Compare the Temporal Change in the Relativistic Electron Flux With Data Sets of ULF Indices, Solar Wind Variables, and Geomagnetic Indices, Separately and in Combination[a]

		ULF Indices		Solar Wind				Geomagnetic Indices		
		$<S_{grd}>$*	$<S_{geod}>$*	$<v_{sw}>$*	$<n>$*	$<\log(S_p)>$*	$<\sin^2(\theta_{clock})>$*	$<\log(AE)>$*	$<Kp>$*	r_{corr}
1	ΔF_{12hr}	1.72	−1.41							0.171
2	ΔF_{12hr}			0.21	−0.67	0.26	−0.03			0.283
3	ΔF_{12hr}							−0.25	1.21	0.037
4	ΔF_{12hr}	2.20	−1.19					−1.05	0.22	0.194
5	ΔF_{12hr}	0.28	−0.32	0.26	−0.56	0.24	−0.06			0.287
6	ΔF_{12hr}	0.66	−0.04	0.32	−0.58	0.22	0.22	−0.88	−0.04	0.307
7	ΔF_{96hr}	1.09	−0.10							0.362
8	ΔF_{96hr}			0.54	0.25	0.64	0.25			0.405
9	ΔF_{96hr}							0.10	0.91	0.334
10	ΔF_{96hr}	1.24	−0.08					−0.19	−0.01	0.364
11	ΔF_{96hr}	0.25	0.19	0.07	0.13	0.70	0.07			0.412
12	ΔF_{96hr}	0.36	0.32	0.09	0.08	0.67	0.10	−0.09	−0.20	0.413

[a]The CCA coefficients (weights) are collected in the table for those various combinations. Rows 1–6 correspond to the 12 h change ΔF_{12hr} of the flux and rows 7–12 correspond to the 96 h change ΔF_{96hr} of the flux.

proton-specific entropy of the solar wind $S_p = T_p/n_p^{2/3}$ has been added to the solar wind data set; it will be found that the proton-specific entropy of the solar wind is an important factor for the radiation belt flux. Rows 1–6 pertain to the 12 h change ΔF_{12hr} in the value of the flux (shorter-term) and rows 7–12 pertain to the 96 h change ΔF_{96hr} in the flux (longer term). The column labels in Tables 9 and 10 all have the notation $<X>$, meaning that the variable X in the column is averaged over the previous 12 or 96 h as appropriate for ΔF_{12hr} or for ΔF_{96hr}. The final column in Tables 9 and 10 displays the canonical correlation coefficient $r_{(1)}$ between ΔF and the maximum correlation vector $V_{(1)}$.

Table 10 provides information about which variables contribute information to the maximum correlation vector $V_{(1)}$ with coefficients (weights) given in Table 9. (Before examining the individual correlations, note in Table 10 that the canonical correlations (last column) are systematically lower for ΔF_{12hr} (rows1–6) than they are for ΔF_{96hr} (rows 7–12).) Rows 1–6 for the 12 h change ΔF_{12hr} in the flux will be examined first. Looking at row 1 of Table 10, it is seen that the maximum correlation vector $V_{(1)}$ strongly favors S_{grd} over S_{geod}. In row 2, n is the most favored solar wind variable. Note in row 3 that $r_{(1)}$ is equal to only 0.037 between the maximum correlation vector $V_{(1)}$ and ΔF_{12hr}: log(AE) and Kp provide essentially no information about the behavior of ΔF_{12hr}. As the various data sets are put together (rows 4–6), the resulting maximum correlation vector relies most strongly on n of the solar wind. In particular in row 6, the highest correlation with the canonical variable describing ΔF_{12hr} is an anticorrelation with the solar wind density n with a correlation coefficient of −85.9%. Note also in row 6 that S_{grd} is favored over S_{geod} in the variable $V_{(1)}$ for describing the variance of ΔF_{12hr}, but

Table 10. For the Various Combinations of CCA Analysis in Table 9, the Correlation Coefficients (Loadings) Between the Individual Input Variables and the Canonical Variables to Which They Belong

		ULF Indices		Solar Wind				Geomagnetic Indices		
		$<S_{grd}>$*	$<S_{geod}>$*	$<v_{sw}>$*	$<n>$*	$<\log(S_p)>$*	$<\sin^2(\theta_{clock})>$*	$<\log(AE)>$*	$<Kp>$*	r_{corr}
1	ΔF_{12hr}	57.0%	−1.4%							0.171
2	ΔF_{12hr}			73.4%	−93.2%	83.1%	−0.9%			0.283
3	ΔF_{12hr}							80.1%	99.2%	0.037
4	ΔF_{12hr}	50.2%	−1.2%					15.4%	19.1%	0.194
5	ΔF_{12hr}	34.1%	−0.8%	72.4%	−92.0%	82.1%	−0.9%			0.287
6	ΔF_{12hr}	31.8%	−0.8%	67.6%	−85.9%	76.6%	−0.8%	9.8%	12.1%	0.307
7	ΔF_{96hr}	99.9%	85.4%							0.362
8	ΔF_{96hr}			89.5%	−53.2%	91.8%	26.9%			0.405
9	ΔF_{96hr}							90.8%	99.9%	0.334
10	ΔF_{96hr}	99.5%	85.0%					83.3%	91.6%	0.364
11	ΔF_{96hr}	87.8%	75.1%	88.0%	−52.3%	90.2%	26.4%			0.412
12	ΔF_{96hr}	87.6%	74.9%	87.7%	−52.2%	90.2%	26.4%	73.3%	80.7%	0.413

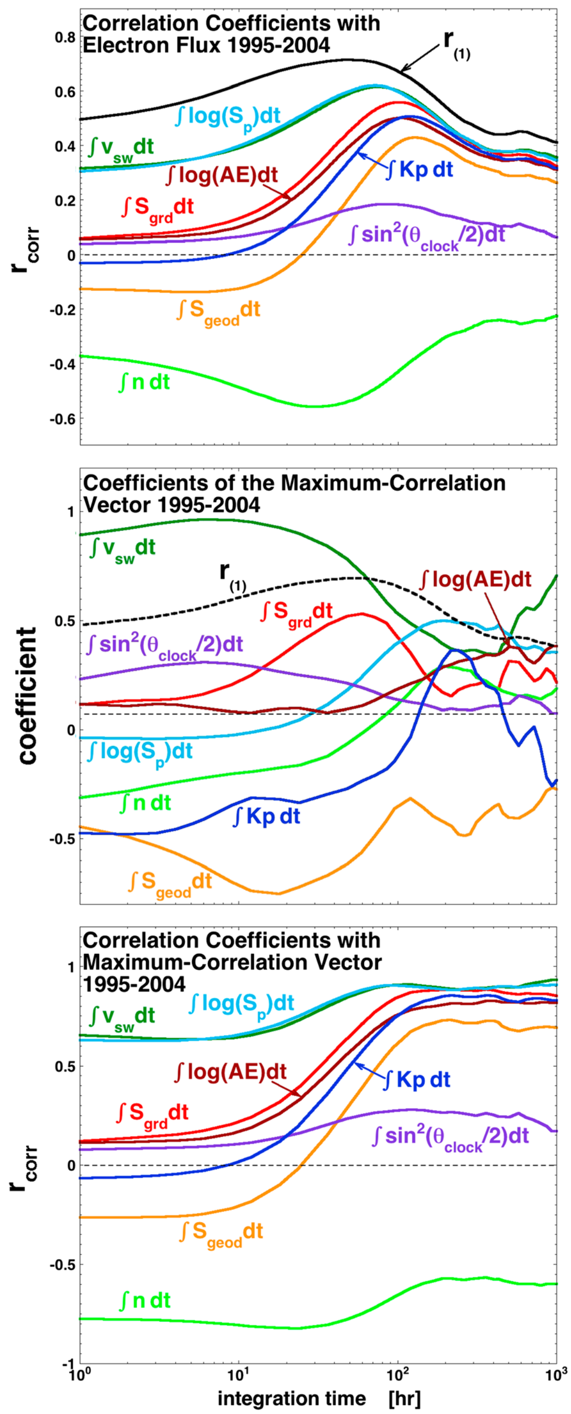

Figure 6. (top) Pearson linear correlation coefficients between the relativistic-electron flux F and time integrals of various solar wind parameters, geomagnetic indices, and ULF indices are plotted as a function of the integration time into the past. (middle) The coefficients (weights) of the CCA-generated variable $V_{(1)}$ are plotted as a function of the integration time of the input variables. (bottom) The correlation coefficients (loadings) between the input variables and $V_{(1)}$ are plotted as a function of the integration time of the input variables.

that the correlation is nowhere near the magnitude of −85.9% for n. We can speculate that this strong anticorrelation between the 12 h change in the relativistic-electron flux ΔF_{12hr} and the solar wind number density n averaged over those 12 h represents, in part, rapid dropouts of the electron flux when the solar wind density increases to high levels [*Onsager et al.*, 2007; *Borovsky and Denton*, 2010a] and rapid recoveries of the flux after the solar wind density subsides [*Borovsky and Denton*, 2009a, 2011]. Note in rows 1–6 of Table 10 that the 12 h change in the relativistic-electron flux is uncorrelated with the IMF clock angle function $\sin^2(\theta_{clock}/2)$ averaged over the previous 12 h.

Information about the 96 h change in the flux appears in rows 7–12 of Table 10. Looking at the $r_{(1)}$ values in the final column of rows 7–9, it is seen that the ULF indices, the solar wind, and the geomagnetic indices all make contributions to describing the variance of ΔF_{96hr}, with the solar wind contribution being the strongest. Note in rows 7–12 of Table 10 that S_{grd} is strongly favored over S_{geod} for describing the variance of ΔF_{96hr}; it is difficult to interpret whether (a) S_{grd} is more physically fundamental to ΔF_{96hr} than S_{geod} is or whether (b) S_{geod} is more noisy than S_{grd}. When all the data sets are combined (row 12), $\log(S_p)$ is the strongest contributor to the maximum correlation vector. The specific entropy S_p is an indicator of the type of solar wind plasma: High S_p indicates coronal-hole-origin plasma and low S_p indicates streamer-belt-origin plasma. In row 12 of Table 10, $V_{(1)}$ describing ΔF_{96hr} has a high correlation with v_{sw} which can be interpreted as heating of the radiation belt by high v_{sw}, $V_{(1)}$ describing ΔF_{96hr} has a high correlation with S_{grd} which can be interpreted as energization of the radiation belt by ULF waves, and $V_{(1)}$ describing ΔF_{96hr} has a high correlation with Kp which could be interpreted as radiation belt energization during high geomagnetic activity (perhaps by substorm injection-driven waves). But in row 12, the correlation with $\log(S_p)$ is the highest, indicating an increase of the relativistic-electron flux during intervals of coronal-hole-origin solar wind plasma and/or a decrease in the relativistic-electron flux during intervals of streamer-belt-origin plasma: Both the increase [*Borovsky and Denton*, 2010b] and the decrease [*Borovsky and Denton*, 2009b] are seen in superposed-epoch views of the

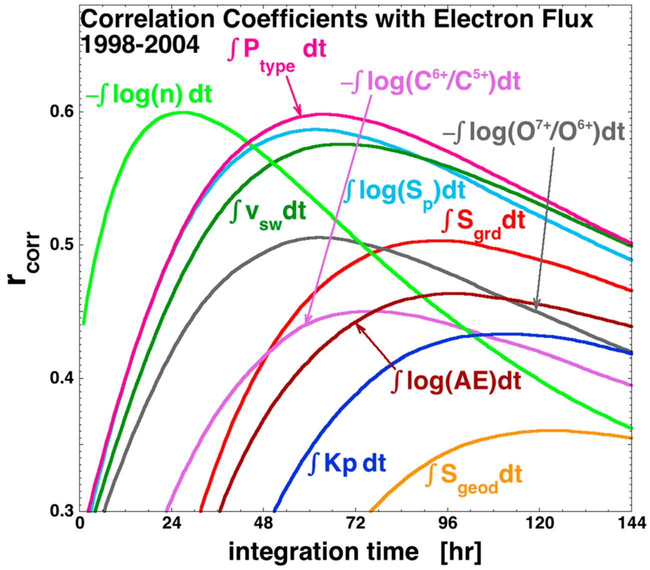

Figure 7. For the years 1998–2004, the Pearson linear correlation coefficients between the relativistic-electron flux F and the time intervals of various solar wind parameters, geomagnetic indices, and ULF and indices are plotted as a function of the integration time into the past.

transition from streamer-belt-origin plasma to coronal-hole-origin plasma.

Note in rows 7–12 of Table 10 the positive correlation between the 96 h average of the clock angle function $\sin^2(\theta_{clock}/2)$ and variable $V_{(1)}$ describing the 96 h change in the relativistic-electron flux ΔF_{96hr}. This is the Russell-McPherron effect [*McPherron et al.*, 2009] wherein growth of the radiation belt fluxes is associated with long intervals with the average value of the IMF vector having a southward component. This positive correlation with $\sin^2(\theta_{clock}/2)$ is expected if the energization or the source of the radiation belt depends on geomagnetic activity [e.g., *Obara et al.*, 2000; *Meredith et al.*, 2002] and/or if the decay of the radiation belt depended on a lack of geomagnetic activity [e.g., *Borovsky and Steinberg*, 2006; *Meredith et al.*, 2006; *Borovsky and Denton*, 2009b, 2011].

In comparing the sizes of the coefficients of the input variables in the composite canonical variables (the "weights") in Table 9 with the sizes of the correlation coefficients between the input variables and the canonical variables (the "canonical loadings") in Table 10, one of two effects can sometimes occur [cf. *MacKinnon et al.*, 2000; *Nimon et al.*, 2010]. When the coefficient (weight) is anomalously small for an input variable compared with its correlation coefficient (canonical loading), it is a sign that there is at least one "confounding" variable in the input variables, with another input variable correlated with the confounding variable [*Robins*, 1989; *Frank*, 2000]; the variable with the anomalously small weight (which may be the confounding variable or may be a confounded variable) has some of its contribution to the canonical variable shared by another input variable. Hence, its weight is reduced. On the contrary, when the coefficient (weight) for an input variable is anomalously large compared with its correlation coefficient (canonical loading), it is a sign that that input variable is playing a "suppression" role; specifically, the variable is acting to cancel out (suppress) the irrelevant variance of other input variables in order to improve the overall correlations [*Conger*, 1974; *Tzelgov and Henik*, 1991].

An example of suppression can be seen in row 1 of Table 9 where the coefficient (−1.41) of $<S_{geod}>^*$ is large relative to its correlation coefficient (−1.4%) in row 1 of Table 10. Since $<S_{grd}>^*$ is the only other input variable in row 1, $<S_{geod}>^*$ is acting to suppress $<S_{grd}>^*$. Specifically, $<S_{geod}>^*$ is being used to subtract off variance in $<S_{grd}>^*$ that is not related to the variance in ΔF_{96hr}. Note that it is slow variance that is being subtracted off since $<S_{geod}>^*$ and $<S_{grd}>^*$ are 12 h averages in row 1. This suppression effect can be seen again for the coefficient of $<S_{geod}>^*$ in rows 4 and 5 of Table 9.

Another example of suppression can be seen in row 6 of Table 9 where the coefficient (−0.88) of $<\log(AE)>^*$ is large relative to the correlation coefficient (9.8%) in row 6 of Table 10. Unlike the case of row 1, it is difficult to discern what input variables $<\log(AE)>^*$ might be suppressing.

An example of shared variance and reduced weights can be seen in row 9 of Tables 9 and 10 where the coefficient (0.10) of $<\log(AE)>^*$ is anomalously low compared with its correlation (90.8%).

In Figure 6 (top), some Pearson linear correlation coefficients between the multispacecraft-averaged relativistic-electron flux F at geosynchronous orbit and various time integrals of the ULF indices S_{grd} and S_{geod}, the solar wind parameters v_{sw}, n, $\log(S_p)$, and $\sin^2(\theta_{clock}/2)$, and the geomagnetic indices $\log(AE)$ and Kp are plotted in color as functions of the integration time. The time integrations are into the past with respect to the time at which the relativistic-electron flux F is measured. For instance, an integration time of 1 h on v_{sw}

uses the 1 h of v_{sw} data at the same time as the flux; an integration time of 45 h on v_{sw} uses the same hour of v_{sw} data plus the previous 44 h of v_{sw} data to perform the integration on v_{sw}, and that 45 h integration of v_{sw} is compared with the 1 h of flux to perform the correlation. The correlations with F all peak at integration times of 30–120 h. The strongest correlation with F is for $\int \log(S_p)\,dt$ integrated over the previous 72 h, where S_p is the proton-specific entropy of the solar wind plasma. $\int \log(S_p)\,dt$ for 72 h being high is an indicator that there has been coronal-hole-origin plasma for the previous 72 h and $\int \log(S_p)\,dt$ being low is an indicator that there has been streamer-belt-origin plasma for the previous 72 h. Putting the quantities S_{grd}, S_{geod}, v_{sw}, n, $\log(S_p)$, $\sin^2(\theta_{clock}/2)$, $\log(AE)$, and Kp into CCA with F yields, for every integration time, a canonical correlation vector $V_{(1)}$: The canonical correlation coefficient $r_{(1)}$ between $V_{(1)}$ and F is plotted in black in Figure 6 (top). Note that the magnitude of $r_{(1)}$ exceeds the magnitude of any individual correlation. Note also in image that there is a weak localized peak in all quantities at an integration time corresponding to the solar rotation period of 27 days (648 h).

In Figure 6 (middle), the coefficients (weights) of the canonical vector $V_{(1)}$ are plotted as a function of the integration time. The coefficients in Figure 6 (middle) can be related to the individual correlations in Figure 6 (top), but not always. For examples, note the difference in the behavior of the curves for $\int n\,dt$ and $\int S_{geod}\,dt$ in the two plots. Cross correlations between the various input variables weigh heavily on CCA's choice of coefficients for $V_{(1)}$. The canonical correlation coefficient $r_{(1)}$ between F and $V_{(1)}$ is also plotted as the black dashed curve in Figure 6 (middle): $r_{(1)}$ peaks at a value of 0.695 at an integration time of 52 h. At 52 h, the canonical variable $V_{(1)}$ that describes the flux is

$$\begin{aligned} V_{(1)} = {} & 0.552\int^{52hr} S_{grd}{}^*dt - 0.593\int^{52hr} S_{geod}{}^*dt + 0.764\int^{52hr} v_{sw}{}^*dt \\ & - 0.049\int^{52hr} n^*dt + 0.203\int^{52hr} \log(S_p)^*dt \\ & + 0.209\int^{52hr} \sin^2(\theta_{clock}/2)^*dt + 0.098\int^{52hr} \log(AE)^*dt \\ & - 0.258\int^{52hr} Kp^*dt \end{aligned} \tag{4}$$

where the correlation coefficient between $V_{(1)}$ as given by expression (4) and the flux F is $r_{(1)} = 0.695$.

In Figure 6 (bottom), the Pearson linear correlation coefficients (loadings) between the individual integrals and the canonical correlation vector $V_{(1)}$ are plotted. These correlations are related to the correlations with F in Figure 6 (top), but not exactly since CCA accounts for cross correlations of the integrals when choosing the coefficients for $V_{(1)}$. Note in Figure 6 (bottom) that $\int n\,dt$ dominates the correlation with $V_{(1)}$ at integration times of ~30 h and that $\int \log(S_p)\,dt$ and $\int v_{sw}\,dt$ dominate the correlation with $V_{(1)}$ at longer integration times.

If in the CCA process only the time integrals of S_{grd} and S_{geod} are given as input variables to match with the instantaneous relativistic-electron flux, then the maximum canonical correlation is obtained for an integration time of 69 h and the canonical variable $V_{(1)}$ that describes the flux is

$$V_{(1)} = 1.740\int^{69hr} S_{grd}{}^*dt - 0.990\int^{69hr} S_{geod}{}^*dt \tag{5}$$

the canonical correlation coefficient between $V_{(1)}$ and the flux F is $r_{(1)} = 0.598$ for the integration time of 69 h. The quantity $1.740S_{grd}{}^* - 0.990S_{geod}{}^*$ is a constant times the difference quantity $S_{grd}{}^* - 0.569S_{geod}{}^*$: Using the values in Table 4 to convert $S_{grd}{}^*$ into S_{grd} and $S_{geod}{}^*$ into S_{geod}, the quantity $S_{grd}{}^* - 0.569S_{geod}{}^*$ can be written as $S_{grd} - 0.693S_{geod}$. This is where the difference ULF index $\Delta S_{mag} \equiv S_{grd} - 0.693S_{geod}$ is defined. For the ULF indices S_{grd} and S_{geod}, the maximum correlation with F is with $\int^{69hr} \Delta S_{mag}\,dt = \int^{69hr} (S_{grd} - 0.693S_{geod})\,dt$. (Note that this maximum correlation for $\int^{69hr} \Delta S_{mag}\,dt$ at an integration time of 69 h could be a compromise between $\int S_{grd}\,dt$ at one integration time minus $\int S_{geod}\,dt$ at another integration time.)

In Figure 6 (middle), the largest correlations found with the relativistic-electron flux F were for integrals of the proton-specific entropy S_p of the solar wind; likewise in Tables 9 and 10, the proton-specific entropy dominated the correlations with the 96 h change ΔF_{96hr} of the relativistic-electron flux. This can be interpreted as the importance of intervals of solar wind type to the state of the relativistic-electron flux.

To further explore this, the correlations of the flux F with the heavy-ion charge-state ratios of the solar wind are examined in Figure 7 and the identification of solar wind plasma by specific entropy and charge-state ratios is examined in Figure 8. Hourly averages of the charge-state density ratios C^{6+}/C^{5+} (=number density of carbon 6+ ions in the solar wind divided by the number density of carbon 5+ ions in the solar wind) and

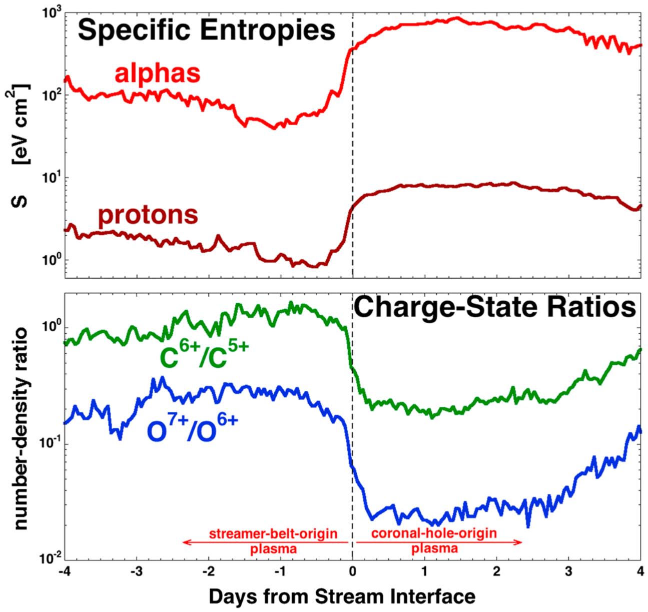

Figure 8. For the superposition of 27 corotating interaction regions with the zero epoch chosen to be the passage of the CIR stream interface, (top) the superposed average of the alpha-particle and proton-specific entropies are plotted as a function of time from the stream interfaces and (bottom) the superposed average of the carbon-ion charge-state ratio and the oxygen-ion charge-state ratio are plotted as a function of time from the stream interfaces.

O^{7+}/O^{6+} (=number density of oxygen 7+ ions in the solar wind divided by the number density of oxygen 6+ ions in the solar wind) are available from ACE SWICS starting in the year 1998. For overlap with the ULF indices, the years 1998–2004 are examined in Figure 7. For those years, the correlation coefficients between the multisatellite-averaged relative-electron flux F and integrals into the past of $-\log(C^{6+}/C^{5+})$, $-\log(O^{7+}/O^{6+})$, S_{grd}, S_{geod}, v_{sw}, $-\log(n)$, $\log(S_p)$, Kp, and $\log(AE)$ are plotted as functions of the integration time. Note the correlation behavior of $-\log(C^{6+}/C^{5+})$ and $-\log(O^{7+}/O^{6+})$ are similar to that of $\log(S_p)$, but their correlations with F are not as strong.

In Figure 8, the proton- and alpha particle-specific entropies of the solar wind plasma (top) and the oxygen and carbon charge-state ratios of the solar wind plasma (bottom) are plotted as a function of time in superposed averages of 27 corotating interaction regions (CIRs). The 27 CIRs from the years 2003–2008 are listed in Table 1 of *Borovsky and Denton* [2010c]. The CIRs were picked with three criteria: (1) that they have a clear, dominant shear zone as seen in the local-Parker-spiral coordinate system [cf. *Borovsky and Denton*, 2010c, section 3], (2) that they do not contain interplanetary shocks, and (3) that they are followed by long (~3 days or more) intervals of high-speed (>600 km/s) wind. For the superposed-epoch analysis of Figure 8, the zero epoch for the averaging is triggered on the CIR stream interface, identified as the maximum of the out-of-ecliptic-plane component of the plasma vorticity in each CIR [cf. *Borovsky and Denton*, 2010c, section 3]. The CIR stream interface is believed to map to the coronal-hole boundary on the solar surface separating plasma of coronal-hole origin from plasma of streamer-belt origin [cf. *Forsyth and Marsch*, 1999; *Gosling and Pizzo*, 1999; *Crooker et al.*, 2010; *Foullon et al.*, 2011], with the solar wind plasma after the stream interface being of coronal-hole origin and the solar wind plasma before the stream interface being of either helmet-streamer-origin plasma or pseudostreamer-origin plasma [*Borovsky and Denton*, 2013]. The plasma before the stream interface can also be mixed with ejecta, which also has low specific entropy and high charge-state ratios; it is expected that ejecta should appear near the magnetic field sector reversals [e.g., *Mendoza and Perez-Enriquez*, 1993; *Srivastava et al.*, 1997; *Foullon et al.*, 2011], which precede the stream interface [*Gosling et al.*, 1978]. This plasma transition at the stream interface is marked at the bottom of Figure 8 (bottom). In Figure 8 (top), the proton-specific entropy $S_p = T_p/n_p{}^{2/3}$ (as measured with the Solar Wind Electron Proton Alpha Monitor plasma instrument [*McComas et al.*, 1998] on ACE) is plotted logarithmically in dark red and the alpha particle-specific entropy $S_\alpha = T_\alpha/n_\alpha{}^{2/3}$ (as measured with the SWICS instrument [*Gloeckler et al.*, 1998] on ACE) is plotted logarithmically in red. Note the strong transitions in both curves from lower specific entropy in the streamer-belt-origin plasma to the higher specific entropy in the coronal-hole-origin plasma. In Figure 8 (bottom), the C^{6+}/C^{5+} (green) and O^{7+}/O^{6+} (blue) charge-state ratios (both measured with the SWICS instrument on ACE) are plotted logarithmically. Note the strong transitions in both curves from higher charge-state ratios (indicating hotter plasma at the Sun) in the streamer-belt-origin plasma to the lower charge-state ratios (indicating cooler plasma at the Sun) in the coronal-hole-origin plasma.

Any one of the four quantities plotted in Figure 8 could be used as an indicator of the type of solar wind plasma [e.g., *Burlaga et al.*, 1990; *Siscoe and Intriligator*, 1993; *Geiss et al.*, 1995; *von Steiger et al.*, 2000; *Zurbuchen et al.*, 2002; *Lazarus et al.*, 2003; *Pagel et al.*, 2004; *Zhao et al.*, 2009; *Landi et al.*, 2012]. A better (less noise) indicator would be $\log(S_p) + \log(S_\alpha) - \log(C^{6+}/C^{5+}) - \log(O^{7+}/O^{6+})$. If the alpha particle temperature or density is not available, then the quantity $2\log(S_p) - \log(C^{6+}/C^{5+}) - \log(O^{7+}/O^{6+})$ can be used. Using $\log(A) + \log(B) = \log(AB)$, this latter expression can also be written as $\log(S_p{}^2C^{5+}O^{6+}/C^{6+}O^{7+})$. Defining the quantity

$$P_{\text{type}} \equiv 2\log(S_p) - \log(C^{6+}/C^{5+}) - \log(O^{7+}/O^{6+}) \quad (6)$$

as an indicator of the type of solar wind plasma, P_{type} is high in coronal-hole-origin solar wind and the quantity is low in streamer-belt-origin solar wind. In Figure 7, the correlation of the integral of $P_{\text{type}} = 2\log(S_p) - \log(C^{6+}/C^{5+}) - \log(O^{7+}/O^{6+})$ with the relativistic-electron flux F in the years 1998–2004 is plotted in pink as a function of the integration time. Note that the relativistic-electron flux F has the highest correlation with this indicator of the type of solar wind plasma, peaking at $r_{corr} = 0.598$ at an integration time of 64 h. The interpretation is that the flux F tends to be high after an interval of coronal-hole plasma and the flux tends to be low after an interval of streamer-belt-origin plasma.

Various studies have directly or indirectly connected the dynamics of the relativistic-electron flux of the magnetosphere with the velocity of the solar wind [e.g., *Paulikas and Blake*, 1979; *Fung and Tan*, 1998; *Desorgher et al.*, 1998; *Vassiliadis et al.*, 2002; *Borovsky and Denton*, 2006; *Reeves et al.*, 2011], with the number density of the solar wind [*Balikhin et al.*, 2011; *Boynton et al.*, 2013], with ULF wave intensities in the magnetosphere [e.g., *Rostoker et al.*, 1998; *Mathie and Mann*, 2000; *Friedel et al.*, 2002; *Nakamura et al.*, 2002; *Kozyreva et al.*, 2007; *Romanova and Pilipenko*, 2009], and with geomagnetic activity [*Baker et al.*, 1999; *Buhler and Desorgher*, 2002; *Lam*, 2004; *Lam et al.*, 2009; *McPherron et al.*, 2009]. In the paragraphs above, we have connected the relativistic-electron flux to the type of solar wind plasma. Using the CCA technique, we will compare simultaneously all of these connections to the relativistic-electron flux F for the years 1998–2004; since all variables will be standardized, all of the connections will be on the same footing during the comparison. For the speed of the solar wind, the integral $\int v_{sw}\,dt$ has its highest correlation with F when the integration time is 68 h (for the years 1998–2004). $\int\log(n)\,dt$ has its highest correlation with F for an integration time of 27 h; $\int(S_{grd} - 0.693S_{geod})\,dt$ ($=\int\Delta S_{mag}\,dt$) has its highest correlation for 69 h; $\int\log(AE)\,dt$ has its highest correlation for 98 h; $\int\sin^2(\theta_{\text{clock}}/2)\,dt$ has its highest correlation for 80 h; and $\int P_{\text{type}}\,dt$ has its highest correlation for 64 h. Putting these six integrals into CCA with F, the resulting composite variable $V_{(1)}$ that describes F is

$$\begin{aligned} V_{(1)} = & -0.489\int^{27\text{hr}}\log(n)dt + 0.330\int^{64\text{hr}}P_{\text{type}}dt \\ & + 0.207\int^{69\text{hr}}(S_{grd} - 0.693S_{geod})dt + 0.142\int^{98\text{hr}}\log(AE)dt \\ & + 0.099\int^{80\text{hr}}\sin^2(\theta_{\text{clock}}/2)dt + 0.022\int^{68\text{hr}}v_{sw}dt \end{aligned} \quad (7)$$

with a correlation coefficient $r_{(1)} = 0.704$ between $V_{(1)}$ and F. Which variables make the strongest contribution to the canonical variable $V_{(1)}$ is determined by the magnitudes of the correlation coefficients (loadings) r_{corr} between the individual variables and $V_{(1)}$ [*Johnson and Wichern*, 2007]. From strongest correlation to weakest correlation, those correlations are −85.2% for $\int^{27\text{hr}}\log(n)\,dt$, 85.0% for $\int^{64\text{hr}}P_{\text{type}}\,dt$, 81.8% for $\int^{68\text{hr}}v_{sw}\,dt$, 80.5% for $\int^{69\text{hr}}(S_{grd} - 0.693S_{geod})\,dt = \int^{69\text{hr}}\Delta S_{mag}\,dt$, 65.9% for $\int^{98\text{hr}}\log(AE)\,dt$, and 24.6% for $\int^{80\text{hr}}\sin^2(\theta_{\text{clock}}/2)\,dt$. The 27 h integral of the logarithm of the solar wind number density makes the strongest contribution and the 64 h integral of the type of solar wind makes nearly the same contribution. In any combination of input variables used for CCA with F, the contribution of $\int^{27\text{hr}}\log(n)\,dt$ is greatest with the contribution of $\int^{64\text{hr}}P_{\text{type}}\,dt$ a very close second. A simplified set of input variables that does nearly as well as expression (7) at describing F is

$$\begin{aligned} V_{(1)} = & -0.599\int^{27\text{hr}}\log(n)dt + 0.598\int^{64\text{hr}}P_{\text{type}}dt \\ & + 0.173\int^{80\text{hr}}\sin^2(\theta_{\text{clock}}/2)dt \end{aligned} \quad (8)$$

which has a correlation coefficient of $r_{(1)} = 0.688$ with F. For expression (8), the correlation of $\int^{27\text{hr}}\log(n)\,dt$ with $V_{(1)}$ is −87.1%, the correlation of $\int^{64\text{hr}}P_{\text{type}}\,dt$ with $V_{(1)}$ is 86.9%, and the correlation of $\int^{80\text{hr}}\sin^2(\theta_{\text{clock}}/2)\,dt$ with $V_{(1)}$ is 25.1%.

6. Integrating the ULF Indices Into the System of Earth Variables

To understand the full reaction of the magnetosphere to the solar wind, variables that describe the state of the magnetospheric system are in demand. Combining the set of geomagnetic indices and the magnetospheric ULF indices, the following Earth vector of values (AE, AL, AU, PCI, Kp, MBI, Dst*, S_{grd}, S_{geod}) is potentially available at every instant of time.

When comparing the multivariable Earth data set to the multivariable solar wind data set, canonical correlation analysis yields a vector of coefficients that when dot producted with the Earth vector yields a single composite Earth variable $E_{(1)}$ that maximizes the correlation with the solar wind data set. Likewise, CCA yields another vector of coefficients that converts the vector of solar wind variables into a single composite solar wind variable $S_{(1)}$ that has the highest correlation with $E_{(1)}$.

To produce this pair of variables $E_{(1)}$ and $S_{(1)}$, a large number of solar wind variables were utilized simultaneously in the CCA process matched up with the Earth vector (AE, AL, AU, PCI, Kp, MBI, Dst*, S_{grd}, S_{geod}) and solar wind variables were eliminated one by one if their contribution to the canonical correlation was negligible. This results in a more manageable, more practical, and more significant solar wind variable. Through this process of elimination, the following pair of variables resulted:

$$E_{(1)} = 0.176\log(AE_1)^* + 0.036AU_1{}^* + 0.039AL_1{}^* + 0.244\mathrm{PCI}_0{}^* + 0.166Kp_1{}^* - 0.235\mathrm{MBI}_1{}^* - 0.236Dst_2{}^{**} + 0.057S_{grd1}{}^* + 0.048S_{geod1}{}^* \quad (9a)$$

$$S_{(1)} = 0.752\log(nv^2)^* - 0.535\log(n)^* - 0.357B_z{}^* + 0.274 <\sin^2(\theta_{\mathrm{clock}}/2)>_3{}^* + 0.233\int^{22\mathrm{hr}} R_{\mathrm{quick}}\mathrm{d}t^* + 0.189B_{mag}{}^* + 0.087<\theta_{Bn}>_3{}^* - 0.070\log(M_A)^* + 0.064\log(F_{10.7})^* \quad (9b)$$

with a canonical correlation coefficient of $r_{(1)} = 0.926$ between $S_{(1)}$ and $E_{(1)}$ for the 1991–2004 data set of hourly values. The asterisk after each variable in expressions (9a) and (9b) indicates that that variable is standardized to have zero mean and a standard deviation of unity as evaluated in the 1995–2004 hourly data set; note that the pressure-corrected Dst* index has two asterisks. In expression (9a), the subscript number indicates the number of hours that the value of the geomagnetic index is lagged from the solar wind values. In expression (9b), $< >_3$ means a 3 h average using the hour at which all solar wind parameters are evaluated plus the two previous hours (cf. J. E. Borovsky, submitted manuscript, 2013d). With standardized variables going into the CCA process, the solar wind variable $S_{(1)}$ and the Earth variable $E_{(1)}$ both have mean values of approximately 0 and standard deviations of approximately unity.

In expression (9b), the term $\int^{22\mathrm{hr}} R_{\mathrm{quick}}\,\mathrm{d}t^*$ is a time integral (into the past) of the reconnection driver function $R_{\mathrm{quick}} = n^{1/2} v_{sw}{}^2 \sin^2(\theta_{\mathrm{clock}}/2)\, M_A{}^{-1.35}\, [1 + 680 \mathrm{M_A}{}^{-3.30}]^{-1/4}$. The normalization is $\int^{22\mathrm{hr}} R_{\mathrm{quick}}\,\mathrm{d}t^* = [\int 2^{2\mathrm{hr}} R_{\mathrm{quick}}\,\mathrm{d}t - <\int^{22\mathrm{hr}} R_{\mathrm{quick}}\,\mathrm{d}t>]/\sigma(\int 2^{2\mathrm{hr}} R_{\mathrm{quick}}\,\mathrm{d}t)$, where for every hour of data in the data set, the integral of R_{quick} back 22 h is performed. This integral term in $S_{(1)}$ represents the past history of geomagnetic activity (without using a geomagnetic index variable in the solar wind data set) and apparently acts to correct a slight hysteresis in the solar wind driving of the magnetosphere. The inclusion of the $\int^{22\mathrm{hr}} R_{\mathrm{quick}}\,\mathrm{d}t^*$ term in $S_{(1)}$ has two effects: (1) It lowers the amount of Earth response at strong driving and (2) it prevents outlier values of $S_{(1)}$ from going to very low values. This second effect reduces a common nonlinearity in the response of geomagnetic activity to solar wind driver functions wherein as the value of the driver function goes to zero the geomagnetic activity remains nonzero [cf. *Borovsky*, 2013a, Figure 7]. The integration time of 22 h was found to be optimal to produce the maximum improvement of the canonical correlation coefficient between $S_{(1)}$ and $E_{(1)}$: Adjusting the integration time from 1 h to 22 h reduces the unaccounted for variance $1 - r_{(1)}{}^2$ of $E_{(1)}$ from 16.1% to 14.2%.

In Figure 9, 64,910 hourly values of the Earth variable $E_{(1)}$ are plotted in black as a function of the hourly solar wind variable $S_{(1)}$. A 300-point running average of the black points is plotted in blue; the running average shows the relationship between $E_{(1)}$ and $S_{(1)}$ to be nearly linear. A least squares linear regression fit to $E_{(1)}$ as a function of $S_{(1)}$ is plotted in red: That fit is

$$E_{(1)\mathrm{predicted}} = 0.926S_{(1)} - 7.77\times10^{-5} \quad (10)$$

which can be used as a predictor for $E_{(1)}$. With a correlation coefficient $r_{(1)} = 0.926$ between $S_{(1)}$ and $E_{(1)}$, $r_{corr}{}^2 = 85.8\%$ of the variance of $E_{(1)}$ can be accounted for from the variance of $S_{(1)}$, leaving only 14.2% of the variance not predicted.

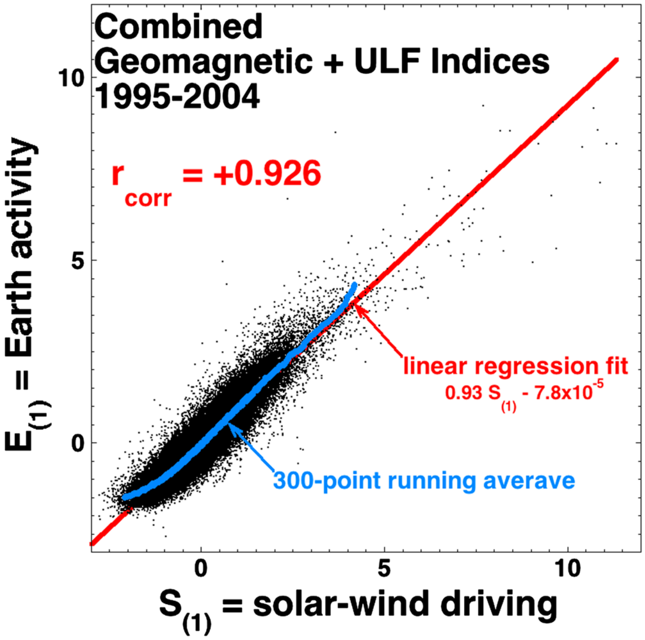

Figure 9. Hourly average values of the canonical Earth variable $E_{(1)}$ (expression (9a)) are plotted as a function of hourly averaged values of the canonical solar wind variable $S_{(1)}$ (expression (9b)).

The autocorrelation functions of the Earth variable $E_{(1)}$ and the solar wind variable $S_{(1)}$ are plotted in Figure 10. The two autocorrelation functions have very similar behaviors. This is unlike the diverse autocorrelation functions of the individual solar wind variables and individual geomagnetic indices in Figure 3. The 1/*e* autocorrelation times for $E_{(1)}$ and $S_{(1)}$ are both 25 h.

In Table 11, the coefficients (weights) of $E_{(1)}$ and $S_{(1)}$ from expressions (9a) and (9b) are collected. Additionally, the correlation coefficients r_{corr} (in percent) of the individual Earth variables and solar wind variables with the two canonical variables $E_{(1)}$ and $S_{(1)}$ are collected. Examining the correlation coefficients of the individual Earth variables with $E_{(1)}$ indicates the strength of the contribution (loading) of each individual Earth variable to $E_{(1)}$. As can be seen in Table 11, the two convective indices MBI and *Kp* make the strongest contributions to $E_{(1)}$. S_{geod}, S_{grd}, and *AU* make the weakest contributions; these weak contributions may imply a lack of predictability to S_{geod}, S_{grd}, and *AU*. Further detrending of S_{geod} and S_{grd} in future by removal of periodic signals may improve their contributions to a canonical Earth variable. Examining in Table 11 the correlation coefficients of the individual solar wind variables with $S_{(1)}$ indicates the strength of the contribution (loading) of each individual solar wind variable to $S_{(1)}$. By this measure, log(*n*) makes essentially no contribution to $S_{(1)}$; in support of this log(*n*) is also uncorrelated with the Earth variable $E_{(1)}$ (Table 11, second column). Note, however, that the coefficient of log(*n*)* (Table 11, third column) is substantial: This is an indication that log(*n*) is playing the role of a suppressor in the CCA process [cf. *Nimon et al.*, 2010]. A suppressor variable improves the correlation between $S_{(1)}$ and $V_{(1)}$ by canceling (suppressing) some of the irrelevant variance in $S_{(1)}$.

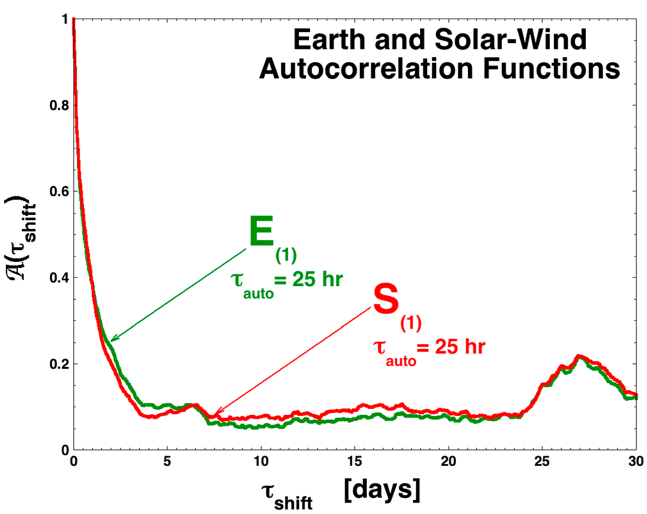

Figure 10. The autocorrelation function of the canonical Earth variable $E_{(1)}$ (expression (9a)) is plotted in green and the autocorrelation function of the canonical solar wind variable $S_{(1)}$ (expression (9b)) is plotted in red. The 1995–2004 data set is used.

The variable $S_{(1)}$ of expression (9b) can also be used to predict the individual geomagnetic indices and ULF indices from the information in the solar wind. As can be seen in Table 11, the Pearson linear correlation coefficients between $S_{(1)}$ and the various indices are 0.796 for log(AE_1), 0.702 for AU_1, 0.746 for $-AL_1$, 0.793 for PCI, 0.832 for Kp_1, 0.876 for $-$MBI$_1$, 0.753 for $-Dst^*_2$, 0.772 for S_{grd1}, and 0.702 for S_{geod1}.

7. Summary

Using cross-correlation analysis, autocorrelation analysis, and canonical correlation analysis, the properties of

Table 11. For the Canonical Correlation Analysis Comparing the Earth Data Set With the Solar Wind Data Set (Expressions (9a) and (9b))[a]

Variable		Coefficient in $E_{(1)}$	Correlation With $E_{(1)}$	Coefficient in $S_{(1)}$	Correlation With $S_{(1)}$
Earth variables	$\log(AE_1)$*	0.176	85.9%		79.6%
	AU_1*	0.036	75.8%		70.2%
	$-AL_1$*	−0.039	80.6%		74.6%
	PCI_0*	0.244	85.6%		79.3%
	Kp_1*	0.166	89.8%		83.2%
	$-\mathrm{MBI}_1$*	0.235	94.6%		87.6%
	$-Dst_2$**	0.236	81.3%		75.3%
	S_{grd1}*	0.057	78.0%		72.2%
	S_{geod1}*	0.048	75.9%		70.2%
Solar wind variables	$\log(nv^2)$*		38.8%	0.752	41.9%
	$\log(n)$*		−0.0%	−0.535	−0.0%
	B_z*		−56.2%	−0.357	−60.6%
	$<\sin^2(\theta_{\mathrm{clock}}/2)>_3$*		53.6%	0.274	57.9%
	$\int^{22\mathrm{hr}} R_{\mathrm{quick}}\, dt$*		68.4%	0.233	73.8%
	B_{mag}*		49.4%	0.189	53.3%
	$<\theta_{Bn}>_3$*		10.9%	0.087	11.8%
	$\log(M_A)$*		−21.9%	−0.070	−23.7%
	$\log(F_{10.7})$*		13.3%	0.064	14.3%

[a]The coefficients (weights) for the Earth variable $E_{(1)}$ are listed in the first column, the coefficients (weights) for the solar wind variable $S_{(1)}$ are listed in the third column, the correlations between the individual input variables and the Earth variable $E_{(1)}$ are listed in the second column, and the correlations between the individual input variables and the solar wind variable $S_{(1)}$ are listed in the fourth column.

the magnetospheric ULF indices were investigated and their connections with solar wind variables, with geomagnetic indices, and with relativistic-electron fluxes were explored. The list of findings of this study is the following:

1. The signal ULF indices S_{gr} and S_{geo} and the total ULF indices T_{gr} and T_{geo} were examined and compared. The signal and total indices are very similar, but the signal indices produce higher correlations with the solar wind and with geomagnetic indices.
2. The ULF indices were detrended to remove 24 h period sine wave signals. The detrended indices are denoted as S_{grd}, S_{geod}, T_{grd}, and T_{geod}. Detrending the ULF indices improves their correlations with each other, with solar wind variables, and with geomagnetic indices.
3. Autocorrelation function analysis shows that there are still very strong 24 h period nonsinusoidal signals in S_{grd} and S_{geod} and a 12 h period signal in S_{geod}. (See also the discussion in section 8.2.) The 24 h signal in S_{grd} is the strongest. Removal of the 24 h period signal in the autocorrelation function of S_{grd} drastically changes the autocorrelation time of S_{grd} and changes the amplitude of the 27 day periodicity in S_{grd}.
4. Research and removal of these nonsinusoidal periodic signals are recommended. Removal of these signals will change the statistical properties of the S_{gr} and S_{geo} indices and will improve their correlations with solar wind parameters (which do not have 12 and 24 h periodicities in them). Removal of these signals is discussed in section 8.2.
5. The ground-based index S_{grd} is more predictable than the geosynchronous index S_{geod} even though S_{grd} has a stronger 24 h periodic signal in it. This may mean that S_{grd} has less noise in it than in S_{geod}, or it may mean that S_{grd} is more physically fundamental than S_{geod}.
6. The ULF indices S_{grd}, S_{geod}, T_{grd}, and T_{geod} react to changes in the solar wind with about a 1 h time lag, as do most geomagnetic indices.
7. The ULF indices S_{grd}, S_{geod}, T_{grd}, and T_{geod} are well correlated with the speed of the solar wind, the IMF clock angle of the solar wind, and the level of magnetic field fluctuations in the solar wind. The geosynchronous indices are sensitive to the level of density fluctuations in the solar wind.
8. The ULF indices S_{grd}, S_{geod}, T_{grd}, and T_{geod} are all strongly correlated with geomagnetic indices. The strongest correlations are with the indices Kp and MBI, which are measures of the strength of convection in the magnetosphere.
9. In the correlative analyses, a difference index $\Delta S = S_{grd} - 0.693 S_{geod}$ repeatedly arises. This difference index produces the highest ULF correlation with the relativistic-electron flux F. The difference index is anticorrelated with the solar wind number density and the difference index is positively correlated with

the strength of high-latitude geomagnetic indices minus the strength of convective geomagnetic indices. The difference index ΔS has very different autocorrelation function properties than those of S_{grd} or of S_{geod}.

10. The multispacecraft-averaged relativistic-electron flux F in the magnetosphere was correlated simultaneously with time integrals of (a) the solar wind velocity, (b) the solar wind number density, (c) the ULF intensity, (d) geomagnetic activity, and (e) the type of solar wind plasma. A solar wind type-of-plasma indicator $P_{\text{type}} \equiv 2\log(S_p) - \log(C^{6+}/C^{5+}) - \log(O^{7+}/O^{6+})$ was defined. The integrals of the solar wind number density $\int n\,dt$ and the type of plasma $\int P_{\text{type}}\,dt$ always dominate the correlations with F. In particular, the solar wind number density dominates the shorter-term behavior of the relativistic-electron flux and the type of plasma dominates the longer-term behavior. The interpretation of the $\int P_{\text{type}}\,dt$ positive correlations with F is that the radiation belt flux F slowly increases during long intervals of coronal-hole-origin solar wind and F slowly decreases during long intervals of streamer-belt-origin solar wind. The interpretation of the $\int n\,dt$ negative correlations with F is that the radiation belt flux F rapidly drops out when the solar wind density increases to high levels and the radiation belt flux rapidly recovers after the solar wind density subsides.
11. The ULF indices S_{grd} and S_{geod} do not play a dominant role in the evolution of F. However, if in future the nonsinusoidal periodic signals in universal time are removed from S_{grd} and S_{geod}, then these indices might become dominant in the correlations with F.
12. The ULF indices S_{grd} and S_{geod} were combined with seven geomagnetic indices to produce an Earth data set. With canonical correlation analysis, the Earth data set was correlated with the solar wind data set. A canonical solar wind variable $S_{(1)}$ and a matching canonical Earth variable $E_{(1)}$ were produced. The solar wind canonical variable $S_{(1)}$ can be used as a solar wind driver function to predict $E_{(1)}$ and to predict individual geomagnetic indices and the ULF indices. In predicting hourly averaged values of $E_{(1)}$, only 14.2% of the hourly variance of $E_{(1)}$ is unaccounted for by the hourly variance of $S_{(1)}$.
13. In the canonical Earth variable $E_{(1)}$, S_{grd} and S_{geod} play roles that are weaker, on average, than the roles played by the various geomagnetic indices. Since CCA is acting to find the strongest correlation between the Earth data set and the solar wind data set, the interpretation of this weaker role is that there is less predictability in S_{grd} and in S_{geod} from the solar wind than there is for the various geomagnetic indices.
14. In an appendix, proxy formulas are given to estimate the values of the ULF indices S_{grd}, S_{geod}, T_{grd}, and T_{geod} from values of the geomagnetic indices when the ULF indices are not available.

8. Discussion

The ULF indices show some deficiencies that are probably related to the presence of nonsinusoidal universal time periodic signals in the indices.

8.1. Properties of the Magnetospheric ULF Indices

Examination has found that the magnetospheric ULF indices S_{grd}, S_{geod}, T_{grd}, and T_{geod} are closely connected to geomagnetic indices. In fact, for the ground-based index S_{grd} and the geosynchronous index S_{geod}, the indices are more strongly correlated with some of the geomagnetic indices than they are with each other.

Several times in the investigation of the ULF indices a difference index arose; one such example is $\Delta S_{mag} = S_{grd} - 0.693 S_{geod}$, the time integral of which yields the highest ULF correlations with F. Canonical correlation analysis found that the ULF index difference between S_{grd} and S_{geod} is related to the difference between the magnitudes of high-latitude geomagnetic indices and convective geomagnetic indices. Perhaps this difference in geomagnetic indices is related to the occurrence of substorms.

The correlations between the ULF indices and the multispacecraft-averaged relativistic-electron flux F are weaker than the correlations between other parameters such as the solar wind velocity, number density, and specific entropy and the relativistic-electron flux. This could mean that the ULF indices are, on average, less important for the evolution of the outer electron radiation belt than other factors. Or the poorer correlations could be the result of the 24 h period and 12 h period nonsinusoidal signals in the ULF indices. These periodic signals represent uncorrelated noise in comparison with F, although the time integration of the ULF indices will reduce that noise.

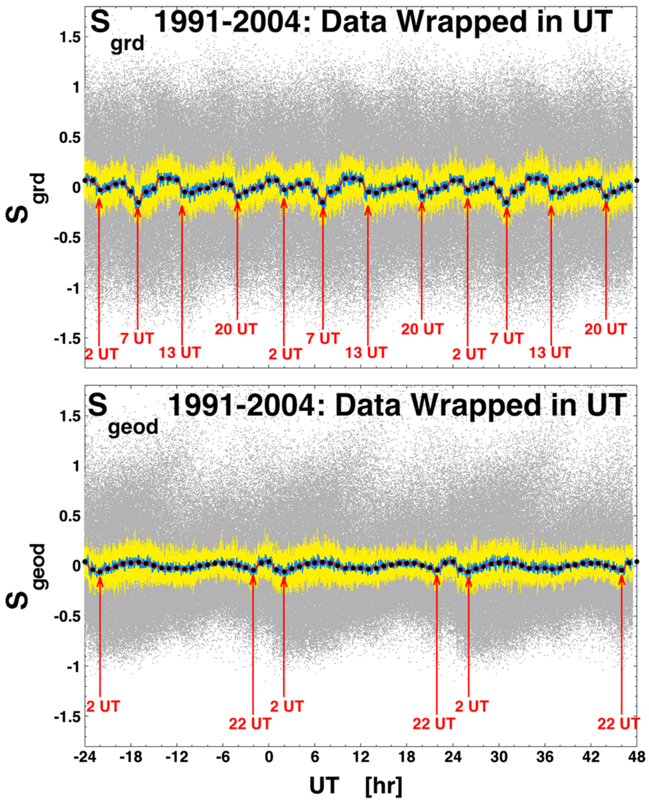

Figure 11. The detrended ULF indices S_{grd} and S_{geod} are plotted in gray with random numbers −0.5 to +0.5 added to the integer values of UT. The data are a repeated for the 24 h before and the 24 h afterward. Running averages of the gray points are plotted: 30-point averages in yellow, 300-point averages in blue, and 3000-point averages in red. The mean values of S_{grd} and S_{geod} for each UT bin are plotted as the larger black points.

The ULF indices S_{grd} and S_{geod} were incorporated into an Earth data set with seven geomagnetic indices. When that Earth data set was matched to the solar wind data set via CCA, the contributions of S_{grd} and S_{geod} to the canonical Earth variable $E_{(1)}$ were found to be modest. CCA determines the coefficients of these canonical variables that maximize the correlation between the two multivariate data sets. The limited size of the contributions of S_{grd} and S_{geod} implies that the ULF indices are not as predictable from the solar wind as other geomagnetic indices are. Removal of the 24 h and 12 h periodic signals from S_{grd} and S_{geod} would undoubtedly make the ULF indices more predictable by the solar wind. Removal of these periodic signals should boost their contribution to the Earth data set.

8.2. Future Work

There are two obvious improvements that can be made to the magnetospheric ULF indices. The first is removal of the 24 h period and 12 h period nonsinusoidal signals that are in the indices. In Figure 11, the hourly values of S_{grd} and S_{geod} for the 1991–2004 data set are plotted in gray as a function of UT, S_{grd} in the top and S_{geod} in the bottom. The data are repeated for the 24 h before and the 24 h afterward and then random numbers from −0.5 to +0.5 are added to the integer UT values to spread the data points horizontally. Running averages of the gray points are also plotted: 30-point running averages in yellow, 300-point running averages in blue, and 3000-point running averages in red. There are about 5000 points per hour of universal time in the plot. The mean values of S_{grd} and S_{geod} for each UT bin are plotted as the larger black points. As can be seen in Figure 11, there are universal time trends to the mean values of S_{grd} and S_{geod}. Some of the repeating features of the mean values are marked with the red arrows in Figure 11. There are larger mean value trends to S_{grd} than to S_{geod} and there are more features. By examining the gray points, it can be seen that the standard deviation (vertical spread) is also universal time dependent for both indices. One can suspect that the skewness and kurtosis of the S_{grd} and S_{geod} distributions also have universal time trends. One straightforward correction to S_{grd} and S_{geod} would be to subtract off the UT-dependent means from the data. A next step would be to consider renormalizing the distribution of values at each UT so that all UT bins have the same standard deviations and skewnesses. The first correction (mean subtraction) will undoubtedly improve the correlations of S_{grd} and S_{geod} with solar wind parameters and with other geomagnetic indices. For S_{geod}, one might also consider performing these renormalizations separately for each of the GOES spacecraft used to construct the geosynchronous ULF index.

The second improvement would be to expand the ULF index data set beyond the year 2004.

In the future, more work connecting the magnetospheric ULF indices to the evolution of the outer electron radiation belt will be performed. In particular, correlations between the ULF indices S_{grd}, S_{geod}, and ΔS_{mag} and the number density n_{rb} and temperature T_{rb} of the radiation belt electrons at geosynchronous orbit [*Denton* *et al.*, 2010; *Borovsky and Denton*, 2011] will be performed. The number density n_{rb} and temperature T_{rb} are indicators of the total number of electrons in the outer electron radiation belt and of the hardness of the spectra of the radiation belt electrons [*Cayton et al.*, 1989; *Belian et al.*, 1996]. The relativistic-electron flux F depends on both n_{rb} and T_{rb} [*Cayton and Belian*, 2007; *Borovsky and Denton*, 2010b], with different physical processes acting on the evolution of n_{rb} than the physical processes acting on the evolution of T_{rb}.

Further work will involve the incorporation of the time derivatives $\partial n_{rb}/\partial t$ and $\partial T_{rb}/\partial t$ of the radiation belt number density n_{rb} and temperature T_{rb} into the Earth data set with S_{grd}, S_{grd}, and the geomagnetic indices.

Appendix A: Proxy Formulas for the ULF Indices S_{gr}, S_{geo}, T_{gr}, and T_{geo}

In the absence of measurements of the ground and geosynchronous ULF indices, approximate values of the indices can be obtained from values of the geomagnetic indices. Here formulas to generate proxy values of the ULF indices are given.

For the S_{gr} and S_{geo} indices, the proxy formulas are

$$S_{grd}{}^* \approx 0.139 AU_0{}^* + 0.023 AL_0{}^* + 0.095 \mathrm{PCI}_{-1}{}^* - 0.328 Kp_0{}^* + 0.027 Dst*_{+1}{}^* - 0.678 \log(AE_0)^* + 0.211 \mathrm{MBI}_0{}^* \quad \text{(A1a)}$$

$$S_{geod}{}^* \approx 0.092 AU_0{}^* + 0.018 AL_0{}^* - 0.114 \mathrm{PCI}_{-1}{}^* + 0.550 Kp_0{}^* + 0.135 Dst*_{+1}{}^* + 0.114 \log(AE_0)^* - 0.317 \mathrm{MBI}_0{}^* \quad \text{(A1b)}$$

Note that in general, AL, Dst*, and MBI are negative quantities. Using the formulas in Table 4, the values of S_{grd}* and S_{geod}* can be converted into S_{grd} and S_{geod}; then using expressions (1a) and (1b), the expressions for S_{grd} and S_{geod} can be converted into S_{gr} and S_{geo}. The linear correlation coefficients between formula values of S_{grd} and actual values of S_{grd} are $r_{corr} = 0.813$ and the linear correlation coefficients between formula values of S_{geod} and actual values of S_{geod} are $r_{corr} = 0.766$.

Likewise, for the T_{gr} and T_{geo} indices, the proxy formulas are

$$T_{grd}{}^* \approx 0.138 AU_0{}^* + 0.0061 AL_0{}^* + 0.108 \mathrm{PCI}_{-1}{}^* - 0.369 Kp_0{}^* + 0.047 Dst*_{+1}{}^* - 0.652 \log(AE_0)^* + 0.208 \mathrm{MBI}_0{}^* \quad \text{(A2a)}$$

$$T_{geod}{}^* \approx 0.090 AU_0{}^* + 0.031 AL_0{}^* - 0.111 \mathrm{PCI}_{-1}{}^* + 0.552 Kp_0{}^* + 0.141 Dst*_{+1}{}^* + 0.098 \log(AE_0)^* - 0.336 \mathrm{MBI}_0{}^* \quad \text{(A2b)}$$

The linear correlation coefficients between formula values of T_{grd} and actual values of T_{grd} are $r_{corr} = 0.791$ and the linear correlation coefficients between formula values of T_{geod} and actual values of T_{geod} are $r_{corr} = 0.745$.

Acknowledgments
The authors wish to thank Jung-Chao Wang for use of a matrix-eigenvalue algorithm. The ULF indices were archived by Augsburg College. This work was supported at the University of Michigan by the NASA Geospace SR&T Program; at the Space Science Institute by the NASA CCMSM-24 Program, the NASA Magnetospheric Guest-Investigator Program, and the NSF GEM Program; and at Lancaster University by Science and Technology Funding Council grant ST/I000801/1.

Yuming Wang thanks the reviewers for their assistance in evaluating this paper.

References

Baker, D. N., R. L. McPherron, T. E. Cayton, and R. W. Klebesadel (1990), Linear prediction filter analysis of relativistic electron properties at 6.6 R_E, *J. Geophys. Res.*, *95*, 15,133–15,140, doi:10.1029/JA095iA09p15133.
Baker, D. N., S. G. Kanekal, T. I. Pulkkinen, and J. B. Blake (1999), Equinoctial and solstitial averages of magnetospheric relativistic electrons: A strong semiannual modulation, *Geophys. Res. Lett.*, *26*, 3193–3196, doi:10.1029/1999GL003638.
Balikhin, M. A., R. J. Boynton, S. N. Walker, J. E. Borovsky, S. A. Billings, and H. L. Wei (2011), Using the NARMAX approach to model the evolution of energetic electrons fluxes at geostationary orbit, *Geophys. Res. Lett.*, *38*, L18105, doi:10.1029/2011GL048980.
Belian, R. D. (1999), Personnel involved with the Synchronous Orbit Particle Analyzer (SOPA) and description of the Charged Particle Analyzer (CPA) detectors, Los Alamos National Laboratory Report LA-UR-99-2832, Los Alamos, N. M.
Belian, R. D., T. E. Cayton, R. A. Christensen, J. C. Ingraham, M. M. Meier, G. D. Reeves, and A. J. Lazarus (1996), Relativistic electrons in the outer-zone: An 11 year cycle; their relation to the solar wind, *AIP Conf. Proc.*, *383*, 13.
Bendat, J. S., and A. G. Piersol (1971), *Random Data: Analysis and Measurement Procedures*, Sect. 4.8.1, John Wiley, New York.
Bevington, P. R., and D. K. Robinson (1992), *Data Reduction and Error Analysis for the Physical Sciences*, 2nd ed., McGraw-Hill, New York.
Beyer, W. H. (Ed.) (1966), *Handbook of Tables for Probability and Statistics*, Sect. IX, Chem. Rubber, Cleveland, Ohio.
Borovsky, J. E. (2008), The rudiments of a theory of solar-wind/magnetosphere coupling derived from first principles, *J. Geophys. Res.*, *113*, A08228, doi:10.1029/2007JA012646.
Borovsky, J. E. (2013a), Physics based solar-wind driver functions for the magnetosphere: Combining the reconnection-coupled MHD generator with the viscous interaction, *J. Geophys. Res. Space Physics*, *118*, 7119–7150, doi:10.1002/jgra.50557.
Borovsky, J. E. (2013b), Physical improvements to the solar wind reconnection control function for the Earth's magnetosphere, *J. Geophys. Res. Space Physics*, *118*, 2113–2121, doi:10.1002/jgra.50110.
Borovsky, J. E., and J. Birn (2014), The solar wind electric field does not control the dayside reconnection rate, *J. Geophys. Res. Space Physics*, *119*, 751–760, doi:10.1002/2013JA019193.
Borovsky, J. E., and M. H. Denton (2006), The differences between CME-driven storms and CIR-driven storms, *J. Geophys. Res.*, *111*, A07S08, doi:10.1029/2005JA011447.

Borovsky, J. E., and M. H. Denton (2009a), Relativistic-electron dropouts and recovery: A superposed-epoch study of the magnetosphere and the solar wind, *J. Geophys. Res.*, *114*, A02201, doi:10.1029/2008JA013128.
Borovsky, J. E., and M. H. Denton (2009b), Electron loss rates from the outer electron radiation belt caused by the filling of the outer plasmasphere: The calm before the storm, *J. Geophys. Res.*, *114*, A11203, doi:10.1029/2009JA014063.
Borovsky, J. E., and M. H. Denton (2010a), The magnetic field at geosynchronous orbit during high-speed-stream-driven storms: Connections to the solar wind, the plasma sheet, and the outer electron radiation belt, *J. Geophys. Res.*, *115*, A08217, doi:10.1029/2009JA015116.
Borovsky, J. E., and M. H. Denton (2010b), On the heating of the outer radiation belt to produce high fluxes of relativistic electrons: Measured heating rates for high-speed-stream-driven storms, *J. Geophys. Res.*, *115*, A12206, doi:10.1029/2010JA015342.
Borovsky, J. E., and M. H. Denton (2010c), Solar-wind turbulence and shear: A superposed-epoch analysis of corotating interaction regions at 1 AU, *J. Geophys. Res.*, *115*, A10101, doi:10.1029/2009JA014966.
Borovsky, J. E., and M. H. Denton (2011), Evolution of the magnetotail energetic-electron population during high-speed-stream-driven storms: Evidence for the leakage of the outer electron radiation belt into the Earth's magnetotail, *J. Geophys. Res.*, *116*, A12228, doi:10.1029/2011JA016713.
Borovsky, J. E., and M. H. Denton (2013), The differences between storms driven by helmet-streamer CIRs and storms driven by pseudostreamer CIRs, *J. Geophys. Res. Space Physics*, *118*, 5506–5521, doi:10.1002/jgra.50524.
Borovsky, J. E., and H. O. Funsten (2003), Role of solar wind turbulence in the coupling of the solar wind to the Earth's magnetosphere, *J. Geophys. Res.*, *108*(A6), 1246, doi:10.1029/2002JA009601.
Borovsky, J. E., and J. T. Steinberg (2006), The "calm before the storm" in CIR/magnetosphere interactions: Occurrence statistics, solar-wind statistics, and magnetospheric preconditioning, *J. Geophys. Res.*, *111*, A07S10, doi:10.1029/2005JA011397.
Borovsky, J. E., M. F. Thomsen, D. J. McComas, T. E. Cayton, and D. J. Knipp (1998), Magnetospheric dynamics and mass flow during the November 1993 storm, *J. Geophys. Res.*, *103*, 26,373–26,394, doi:10.1029/97JA03051.
Boynton, R. J., M. A. Balikhin, S. A. Billings, G. D. Reeves, N. Ganushkina, M. Gadalin, O. A. Amariutei, J. E. Borovsky, and S. N. Walker (2013), The analysis of electron fluxes at geosynchronous orbit employing a NARMAX approach, *J. Geophys. Res. Space Physics*, *118*, 1500–1513, doi:10.1002/jgra.50192.
Buhler, P., and L. Desorgher (2002), Relativistic electron enhancement, magnetic storms, and substorm activity, *J. Atmos. Sol. Terr. Phys.*, *64*, 593–599.
Burlaga, L. F., W. H. Mish, and Y. C. Whang (1990), Coalescence of recurrent streams of different sizes and amplitudes, *J. Geophys. Res.*, *95*, 4247–4255, doi:10.1029/JA095iA04p04247.
Cayton, T. E., and R. D. Belian (2007), Numerical modeling of the synchronous orbit particle analyzer, *Los Alamos National Laboratory Report LA-14335*.
Cayton, T. E., R. D. Belian, S. P. Gary, T. A. Fritz, and D. N. Baker (1989), Energetic electron components at geosynchronous orbit, *Geophys. Res. Lett.*, *16*, 147–150, doi:10.1029/GL016i002p00147.
Conger, A. J. (1974), A revised definition for suppressor variables: A guide to their identification and interpretation, *Educ. Psychol. Meas.*, *34*, 35.
Crooker, N. U., E. M. Appleton, N. A. Schwadron, and M. J. Owens (2010), Suprathermal electron flux peaks at stream interfaces: Signature of solar wind dynamics or tracer for open magnetic flux transport on the Sun?, *J. Geophys. Res.*, *115*, A11101, doi:10.1029/2010JA015496.
Degeling, A. W., R. Rankin, and S. R. Elkington (2011), Convective and diffusive ULF wave driven radiation belt electron transport, *J. Geophys. Res.*, *116*, A12217, doi:10.1029/2011JA016896.
Denton, M. H., J. E. Borovsky, and T. E. Cayton (2010), A temperature and density description of relativistic electrons in the outer radiation belt during geomagnetic storms, *J. Geophys. Res.*, *115*, A01208, doi:10.1029/2009JA014183.
Desorgher, L., P. Buhler, A. Zehnder, E. Daly, and L. Adams (1998), Outer radiation belt variations during 1995, *Adv. Space Res.*, *22*, 83.
Dessler, A. J., and E. N. Parker (1959), Hydromagnetic theory of geomagnetic storms, *J. Geophys. Res.*, *64*, 2239–2252, doi:10.1029/JZ064i012p02239.
Elkington, S. R., M. K. Hudson, and A. A. Chan (2003), Resonant acceleration and diffusion of outer zone electrons in an asymmetric geomagnetic field, *J. Geophys. Res.*, *108*(A3), 1116, doi:10.1029/2001JA009202.
Forsyth, R. J., and E. Marsch (1999), Solar origin and interplanetary evolution of stream interfaces, *Space Sci. Rev.*, *89*, 7.
Foullon, C., et al. (2011), Plasmoid releases in the heliospheric current sheet and associated coronal hole boundary layer evolution, *Astrophys. J.*, *737*, 1.
Frank, K. A. (2000), Impact of confounding variable on a regression coefficient, *Sociol. Methods Res.*, *29*(2), 147–194.
Freeman, J. W. (1964), The morphology of the electron distribution in the outer radiation zone and near the magnetospheric boundary as observed by Explorer 12, *J. Geophys. Res.*, *69*, 1691–1723, doi:10.1029/JZ069i009p01691.
Friedel, R. H. W., G. D. Reeves, and T. Obara (2002), Relativistic electron dynamics in the inner magnetosphere—A review, *J. Atmos. Sol. Terr. Phys.*, *64*, 265.
Fung, S. F., and L. C. Tan (1998), Time correlation of low-altitude relativistic trapped electron fluxes with solar wind speeds, *Geophys. Res. Lett.*, *25*, 2361–2364, doi:10.1029/98GL01717.
Gatignon, H. (2010), *Statistical Analysis of Management Data*, Springer, New York.
Geiss, J., G. Gloeckler, and R. von Steiger (1995), Origin of solar wind from composition data, *Space Sci. Rev.*, *72*, 49.
Gloeckler, G., et al. (1998), Investigation of the composition of solar and interstellar matter using solar wind and pickup ion measurements with SWICS and SWIMS on the ACE spacecraft, *Space Sci. Rev.*, *86*, 497.
Gosling, J. T., and V. J. Pizzo (1999), Formation and evolution of corotating interaction regions and their three dimensional structure, *Space Sci. Rev.*, *89*, 21.
Gosling, J. T., J. R. Asbridge, S. J. Bame, and W. C. Feldman (1978), Solar wind stream interfaces, *J. Geophys. Res.*, *83*, 1401–1412, doi:10.1029/JA083iA04p01401.
Gussenhoven, M. S., D. A. Hardy, and N. Heinemann (1983), Systematics of the equatorward diffuse auroral boundary, *J. Geophys. Res.*, *88*, 5692, doi:10.1029/JA088iA07p05692.
Hair, J. F., W. C. Black, B. J. Babin, and R. E. Anderson (2010), *Canonical Correlation: A Supplement to Multivariate Data Analysis*, Pearson Prentice Hall Publishing, Upper Saddle River, N. J.
Holzer, R. E., and J. A. Slavin (1982), An evaluation of three predictors of geomagnetic activity, *J. Geophys. Res.*, *87*, 2558–2562, doi:10.1029/JA087iA04p02558.
Johnson, R. A., and D. W. Wichern (2007), *Applied Multivariate Statistical Analysis*, 6th ed., Pearson Prentice Hall, Upper Saddle River, N. J.
King, J. H., and N. E. Papitashvili (2005), Solar wind spatial scales in and comparisons of hourly Wind and ACE plasma and magnetic field data, *J. Geophys. Res.*, *110*, A02104, doi:10.1029/2004JA010649.

Kozyreva, O., V. Pilipenko, M. J. Engebretson, K. Yumoto, J. Watermann, and N. Romanova (2007), In search of a new ULF wave index: Comparison of Pc5 power with dynamics of geostationary relativistic electrons, *Planet. Space Sci.*, *55*, 755.

Lam, H.-L. (2004), On the prediction of relativistic electron fluence based on its relationship with geomagnetic activity over a solar cycle, *J. Atmos. Sol. Terr. Phys.*, *66*, 1703.

Lam, M. M., R. B. Horne, N. P. Meredith, and S. A. Glauert (2009), Radiation belt electron flux variability during three CIR-driven geomagnetic storms, *J. Atmos. Sol. Terr. Phys.*, *71*, 1145.

Landi, E., R. L. Alexander, J. R. Gruesbeck, J. A. Gilbert, S. T. Lepri, W. B. Manchester, and T. H. Zurbuchen (2012), Carbon ionization stages as a diagnostic of the solar wind, *Astrophys. J.*, *744*, 100.

Lazarus, A., J. Kasper, A. Szabo, and K. Ogilvie (2003), Solar wind streams and their origins, *AIP Proc.*, *679*, 187.

Liemohn, M. W., J. U. Kozyra, M. F. Thomsen, J. L. Roeder, G. Lu, J. E. Borovsky, and T. E. Cayton (2001), Dominant role of the asymmetric ring current in producing the stormtime *Dst**, *J. Geophys. Res.*, *106*, 10,883–10,904, doi:10.1029/2000JA000326.

MacKinnon, D. P., J. L. Krull, and C. M. Lockwood (2000), Equivalence of the mediation, confounding, and suppression effect, *Prev. Sci.*, *1*, 173.

Mathie, R. A., and I. R. Mann (2000), A correlation between extended intervals of ULF wave power and storm-time geosynchronous relativistic electron flux enhancements, *Geophys. Res. Lett.*, *27*, 3621–3264, doi:10.1029/2000GL003822.

Mathie, R. A., and I. R. Mann (2001), On the solar wind control of Pc5 ULF pulsation power at mid-latitudes: Implications for MeV electron acceleration in the outer radiation belt, *J. Geophys. Res.*, *106*, 29,783–29,796, doi:10.1029/2001JA000002.

McComas, D. J., S. J. Blame, P. Barker, W. C. Feldman, J. L. Phillips, P. Riley, and J. W. Griffee (1998), Solar Wind Electron Proton Alpha Monitor (SWEPAM) for the Advanced Composition Explorer, *Space Sci. Rev.*, *86*, 563.

McPherron, R. L., D. N. Baker, and L. F. Bargatze (1986), Linear filters as a method of real time prediction of geomagnetic activity, in *Solar Wind-Magnetosphere Coupling*, edited by Y. Kamide and J. A. Slavin, 85 pp., Terra Scientific, Tokyo, Japan.

McPherron, R. L., D. N. Baker, and N. U. Crooker (2009), Role of the Russell-McPherron effect in the acceleration of relativistic electrons, *J. Atmos. Sol. Terr. Phys.*, *71*, 1032.

Mendoza, B., and R. Perez-Enriquez (1993), Association of coronal mass ejections with the heliomagnetic current sheet, *J. Geophys. Res.*, *98*, 9365–9370, doi:10.1029/92JA02897.

Menk, F. W., T. K. Yeoman, D. M. Wright, M. Lester, and F. Honary (2003), High-latitude observations of impulse-driven ULF pulsations in the ionosphere and on the ground, *Ann. Geophys.*, *21*, 559.

Meredith, N. P., R. B. Horne, H. H. A. Iles, R. M. Thorne, D. Heynderickx, and R. R. Anderson (2002), Outer zone relativistic electron acceleration associated with substorm-enhanced whistler mode chorus, *J. Geophys. Res.*, *107*(A7), 1144, doi:10.1029/2001JA900146.

Meredith, N. P., R. B. Horne, S. A. Glaurt, R. M. Thorne, D. Summers, J. M. Albert, and R. R. Anderson (2006), Energetic outer zone electron loss timescales during low geomagnetic activity, *J. Geophys. Res.*, *111*, A05212, doi:10.1029/2005JA011516.

Muller, K. E. (1982), Understanding canonical correlation through the general linear model and principal components, *Am. Stat.*, *36*, 342.

Nagai, T. (1988), "Space weather forecast" prediction of relativistic electron intensity at synchronous orbit, *Geophys. Res. Lett.*, *15*, 425–428, doi:10.1029/GL015i005p00425.

Nakamura, R., J. B. Blake, S. R. Elkington, D. N. Baker, W. Baumjohann, and B. Klecker (2002), Relationship between ULF waves and radiation belt electrons during the March 10, 1998, Storm, *Adv. Space Res.*, *30*, 2163.

Newell, P. T., T. Sotirelis, K. Liou, C.-I. Meng, and F. J. Rich (2007), A nearly universal solar wind-magnetosphere coupling function inferred from 10 magnetospheric state variables, *J. Geophys. Res.*, *112*, A01206, doi:10.1029/2006JA012015.

Nimon, K., R. K. Henson, and M. S. Gates (2010), Revisiting interpretation of canonical correlation analysis: A tutorial and demonstration of canonical commonality analysis, *Multivar. Behav. Res.*, *45*, 702.

Obara, T., T. Nagatsuma, M. Den, E. Sagawa, and T. G. Onsager (2000), Effects of the IMF and substorms on the rapid enhancement of relativistic electron in the outer radiation belt during storm recovery phase, *Adv. Space Res.*, *26*, 89.

Onsager, T. G., G. Rostoker, H.-J. Kim, G. D. Reeves, T. Obara, H. J. Singer, and C. Smithtro (2002), Radiation belt electron flux dropouts: Local time, radial, and particle-energy dependence, *J. Geophys. Res.*, *107*(A11), 1382, doi:10.1029/2001JA000187.

Onsager, T. G., J. C. Green, G. D. Reeves, and H. J. Singer (2007), Solar wind and magnetospheric conditions leading to the abrupt loss of outer radiation belt electrons, *J. Geophys. Res.*, *112*, A01202, doi:10.1029/2006JA011708.

Pagel, A. C., N. U. Crooker, T. H. Zurbuchen, and J. T. Gosling (2004), Correlation of solar wind entropy and oxygen ion charge state ratio, *J. Geophys. Res.*, *109*, A01113, doi:10.1029/2003JA010010.

Pahud, D. M., I. J. Rae, I. R. Mann, K. R. Murphy, and V. Amalraj (2009), Ground-based Pc5 ULF wave power: Solar wind speed and MLT dependence, *J. Atmos. Sol. Terr. Phys.*, *71*, 1082.

Paulikas, G. A., and J. B. Blake (1979), Effects of the solar wind on magnetospheric dynamics: Energetic electrons at the synchronous orbit, in *Quantitative Modeling of Magnetospheric Processes*, edited by W. P. Olson, 180 pp., AGU, Washington, D. C.

Reeves, G. D., S. K. Morley, R. H. W. Friedel, M. G. Henderson, T. E. Cayton, G. Cunningham, J. B. Blake, R. A. Christensen, and D. Thomsen (2011), On the relationship between relativistic electron flux and solar wind velocity: Paulikas and Blake revisited, *J. Geophys. Res.*, *116*, A02213, doi:10.1029/2010JA015735.

Robins, J. (1989), The control of confounding by intermediate variables, *Stat. Med.*, *8*, 679–701.

Romanova, N., and V. Pilipenko (2009), ULF wave indices to characterize the solar wind-magnetosphere interaction and relativistic electron dynamics, *Acta Geophys.*, *57*, 158.

Romanova, N., V. Plipenko, N. Crosby, and O. Khabarova (2007), ULF wave index and its possible applications in space physics, *Bulg. J. Phys.*, *34*, 136.

Rostoker, G., H.-L. Lam, and W. D. Hume (1972), Response time of the magnetosphere to the interplanetary electric field, *Can. J. Phys.*, *50*, 544.

Rostoker, G., S. Skone, and D. N. Baker (1998), On the origin of relativistic electrons in the magnetosphere associated with some geomagnetic storms, *Geophys. Res. Lett.*, *25*, 3701–3704, doi:10.1029/98GL02801.

Sckopke, N. (1966), A general relation between the energy of trapped particles and the disturbance field near the earth, *J. Geophys. Res.*, *71*, 3125–3130, doi:10.1029/JZ071i013p03125.

Singer, H. J., C. T. Russell, M. G. Kivelson, E. W. Greenstadt, and J. V. Olsen (1977), Evidence for the control of Pc 3,4 magnetic pulsations by the solar-wind velocity, *Geophys. Res. Lett.*, *4*, 377–379, doi:10.1029/GL004i009p00377.

Singer, H. J., L. Matheson, R. Grubb, A. Newman, and S. D. Bouwer (1996), Monitoring space weather with the GOES magnetometers, *SPIE Proc.*, *2812*, 299.

Singh, A. K., S. Mishra, and R. Singh (2013), ULF wave index as magnetospheric and space-weather parameters, *Adv. Space Res.*, *52*, 1427.

Siscoe, G., and D. Intriligator (1993), Three views of two giant streams: Aligned observations at 1 AU, 4.6 AU, and 5.9 AU, *Geophys. Res. Lett.*, *20*, 2267–2270, doi:10.1029/93GL02488.

Smith, J. P., M. F. Thomsen, J. E. Borovsky, and M. Collier (1999), Solar wind density as a driver for the ring current in mild storms, *Geophys. Res. Lett.*, *26*, 1797–1800, doi:10.1029/1999GL900341.

Srivastava, N., W. D. Gonzalez, and H. S. Sawant (1997), On the association of eruptive prominences, coronal holes, and current sheets with the coronal mass ejections, *Adv. Space Res.*, *20*, 2355.

Takahashi, K., and A. Y. Ukhorskiy (2008), Timing analysis of the relationship between solar wind parameters and geosynchronous Pc5 amplitude, *J. Geophys. Res.*, *113*, A12204, doi:10.1029/2008JA013327.

Tennekes, H., and J. L. Lumley (1972), *A First Course in Turbulence*, MIT Press, Cambridge, Mass.

Thomsen, M. F. (2004), Why Kp is such a good measure of magnetospheric convection, *Space Weather*, *2*, S11044, doi:10.1029/2004SW000089.

Tzelgov, J., and A. Henik (1991), Suppression situations in psychological research: Definitions, implications, and applications, *Psychol. Bull.*, *109*, 524.

Valdivia, J. A., J. Rogan, V. Munoz, B. A. Toledo, and M. Stepanova (2013), The magnetosphere as a complex system, *Adv. Space Sci.*, *51*, 1934.

Vassiliadis, D. (2006), Systems theory for geospace plasma dynamics, *Rev. Geophys.*, *44*, RG2002, doi:10.1029/2004RG000161.

Vassiliadis, D., A. J. Klimas, S. G. Kanekal, D. N. Baker, and R. S. Weigel (2002), Long-term-average, solar cycle, and seasonal response of magnetospheric energetic electrons to the solar wind speed, *J. Geophys. Res.*, *107*(A11), 1383, doi:10.1029/2001JA000506.

Viall, N. M., L. Kepko, and H. E. Spence (2009), Relative occurrence rates and connection of discrete frequency oscillations in the solar wind density and dayside magnetosphere, *Geophys. Res. Lett.*, *114*, A01201, doi:10.1029/2008JA013334.

von Steiger, R., N. A. Schwadron, L. A. Fisk, J. Geiss, G. Gloeckler, S. Hefti, B. Wilken, R. F. Wimmer-Schweingruber, and T. H. Zurbuchen (2000), Composition of quasi-stationary solar wind flows from Ulysses/Solar Wind Ion Composition Spectrometer, *J. Geophys. Res.*, *105*, 27,217–27,238, doi:10.1029/1999JA000358.

Zhao, L., T. H. Zurbuchen, and L. A. Fisk (2009), Global distribution of the solar wind during solar cycle 23: ACE observations, *Geophys. Res. Lett.*, *36*, L14104, doi:10.1029/2009GL039181.

Zurbuchen, T. H., L. A. Fisk, G. Gloeckler, and R. von Steiger (2002), The solar wind composition throughout the solar cycle: A continuum of dynamic states, *Geophys. Res. Lett.*, *29*(9), 1352, doi:10.1029/2001GL013946.

